TITLE PAGE

Title: Simultaneous CRISPR-Cas9-induced double strand breaks are lethal in cancers

Authors and affiliations: Selina Shiqing K. Teh[1†], Akhil Kotwal[2†], Alexis Bennett[1†], Eitan Halper-Stromberg[1], Laura Morsberger[1], Saum Zamani[2], Yanan Shi[2], Alyza Skaist[3], Qingfeng Zhu[3], Kirsten Bowland[1], Hong Liang[1], Ralph H. Hruban[1,3], Chien-Fu Hung[1,3], Robert A. Anders[1], Nicholas J. Roberts[1,3], Robert B. Scharpf[3], Michael Goldstein[2,3]*, Ying S. Zou[1,3]*, and James R. Eshleman[1,3]*

[1]Department of Pathology, The Sol Goldman Pancreatic Cancer Research Center, The Johns Hopkins University School of Medicine, Baltimore, MD, USA

[2]Department of Radiation Oncology and Molecular Radiation Sciences, The Johns Hopkins University School of Medicine, Baltimore, MD, USA

[3]Department of Oncology, The Johns Hopkins University School of Medicine, Baltimore, MD, USA

[†]These authors contributed equally to this work.

Corresponding authors*:

James R. Eshleman, MD, PhD

CRB II 344, 1550 Orleans St, Baltimore, MD 21287

+1 (410) 614-0671; jeshlem@jhmi.edu

Ying S. Zou, MD, PhD

Halsted 281/Nelson 205 Suite, 600 N Wolfe St, Baltimore, MD 21287

+1 (410) 955-8363; yzou19@jhmi.edu

Michael Goldstein, MD, PhD

CRB II 4th Fl, 1550 Orleans St, Baltimore, MD 21287

mgolds33@jhmi.edu

Conflict-of-interest statement: Drs. Teh, Bowland, Roberts, and Eshleman, and Johns Hopkins University have filed a patent application with the USPTO: US19/051,327. Dr. Anders received consulting fees from Bristol Myers Squibb, Gilead, Jazz Pharmaceuticals, GlaxoSmithKline, RAPT Therapeutics, Daiichi Sankyo, and Abbvie. Johns Hopkins University owns equity in Delfi Diagnostics. Dr. Scharpf is a founder of and holds equity in Delfi Diagnostics. He also serves as the Head of Data Science. This arrangement has been reviewed and approved by Johns Hopkins University in accordance with its conflict-of-interest policies.

ABSTRACT

While radiation is an effective oncologic therapy, killing cancer by inducing DNA double-strand breaks (DSBs), it lacks specificity for neoplastic cells. We have previously adapted the CRISPR-Cas9 gene-editing technology as a cancer-specific treatment modality targeting somatic mutations in pancreatic cancer (PC). However, its tumoricidal potential remains unclear, especially in comparison to therapeutic doses of radiation. Here, we demonstrate that CRISPR-Cas9-induced DSBs are significantly more cytotoxic in PCs than a comparable number of radiation-induced DSBs. We observed >90% tumor growth inhibition by targeting 9 sites with cancer-specific single-guide RNAs (sgRNAs). Through both bioinformatics and cytogenetics analyses, we found that CRISPR-Cas9-induced DSBs triggered ongoing chromosomal rearrangements, with 87% of structural variants being novel rather than directly produced from CRISPR-Cas9-induced DSBs, and chromosomal instability (CIN) peaking before cell death. By comparing the cytotoxicity of CRISPR-Cas9- to radiation-induced DSBs, we demonstrate that the number of DSBs required to achieve equitoxic effects was ~3 times higher for radiation than CRISPR-Cas9. Finally, we show that PC cells that had survived CRISPR-Cas9 targeting retained susceptibility to subsequent CRISPR-Cas9-induced DSBs at different genomic sites with >87% growth inhibition. Together, our data support the therapeutic potential of CRISPR-Cas9 as an anti-cancer strategy.

MAIN TEXT

Introduction

Chromosomal instability (CIN) is a hallmark of cancer and can lead to numerical and/or structural chromosomal abnormalities. When cancer cells undergo selective pressure, such as tumor evolution and therapeutic intervention, CIN allows them to have clonal evolution of heterogeneous karyotypes and phenotypically adapt to the selective conditions (1–3). Experimental evidence has linked CIN with therapeutic resistance through the emergence of drug-resistant clones and has been shown to bypass oncogene addiction and facilitate the expansion of oncogene-independent subclones (1–3). However, CIN comes at a fitness cost since not all resulting karyotypes are viable, and extreme CIN, intolerable to cancer cells, is associated with better patient prognosis (4, 5). Studies have shown that increased chromosome mis-segregation leading to high levels of CIN suppressed tumor growth, and this has been suggested as a selective therapeutic strategy to kill cancers (6–8). It appears that for tumors to propagate sustainably, the equilibrium between the tumor-promoting CIN and tumor-suppressive CIN has to be optimal, and that strategies to shift the equilibrium towards cancer cell killing could be leveraged to improve cancer outcomes (1).

Double strand DNA breaks (DSBs) are known to be the most lethal of all DNA lesions (9, 10). This cytotoxicity originates from the DNA damage response that either senses and repairs DSBs, or initiates a permanent exit from the cell cycle via senescence or cell death. Many conventional anti-cancer strategies, such as radiation therapy and some chemotherapies, rely on DNA damage-induced cytotoxicity for cell death (9). Although human cells have multiple DSB repair mechanisms, DSBs remain dangerous to cell survival as they directly disrupt the integrity of the DNA. Erroneous processing of these breaks can lead to genomic rearrangements characteristic of CIN (9–11). One such consequence is the initiation of breakage-fusion-bridge (BFB) cycles, in which broken chromosomes fuse to form a dicentric chromosome. The resulting dicentric

chromosome breaks during anaphase when two centromeres are stretched to opposite poles, generating novel structural variants (SVs) and chromosomes without telomeres. This cycle is continued when the daughter cells contain chromatids without telomeres, which leads to the production of additional novel genomic rearrangements (12–14).

Studies using endonucleases, such as I-*Sce*I and CRISPR-Cas9 that can induce DSBs at specific locations, have shown a positive correlation between increased number of DSBs and growth inhibition (15–17). CRISPR-Cas9-induced DSBs have been associated with chromothripsis (15), chromosomal rearrangements (18, 19), and cytotoxicity (20–22). However, most studies are developing various methods to circumvent toxicity and increase the success rate of gene editing (22–24), with very few exploiting this cytotoxicity for cell killing (20, 25, 26). Recent studies have also reported upregulation of p53 pathway in Cas9-expressing cells and showed that p53 expression inhibited genetic perturbations, suggesting that the *TP53* mutation status must be considered while studying the effect of CRISPR-Cas9-induced DSBs on cytotoxicity (27–29).

We present data supporting the application of CRISPR-Cas9 as a potent anti-cancer strategy against pancreatic cancer (PC) by inducing CIN. PC is the third leading cause of cancer death in the United States with a dismal 5-year survival rate of just 13% (30). More than 90% of PCs are pancreatic ductal adenocarcinomas (PDACs) (31), and approximately 70% of PDACs contain inactivating mutations in *TP53* (32). Radiation therapy, one of the treatment options for PC patients, damages genomic DNA either directly or indirectly by producing free radicals (33). However, we find that the cytotoxicity of DSBs from CRISPR-Cas9 is greater than those from clinically relevant doses of radiation, and these DSBs lead to extreme CIN, designated chromosome catastrophe, and cell death. More broadly, our study highlights the potential of CRISPR-Cas9 as a selective and highly cytotoxic strategy against cancers.

Results

CRISPR-Cas9-induced DSBs inhibit cancer cell growth

We designed multi-target sgRNAs containing 2-16 target sites in the non-coding regions of the human genome to minimize risk of confounding our interpretations with cytotoxicity caused by gene essentiality (Supplemental Table 1, sgRNA design was previously described (26)). Negative controls included two non-targeting sgRNAs (NT and NT2) that have no target sites in the human genome, while positive controls included three sgRNAs that target repetitive elements. An *HPRT1* gene-targeting sgRNA was also designed for functional testing of Cas9 activity, as inactivation of the *HPRT1* gene leads to 6-thioguanine resistance. The number of predicted target sites of each sgRNA is stated within the parentheses; e.g. 52F(3) indicates that this sgRNA has 3 predicted target sites in the human genome, whereas (rep) indicates that this sgRNA targets repetitive elements. We selected two PC cell lines, Panc10.05 and TS0111, which both harbor inactivating *TP53* mutations (homozygous I255N and homozygous C275Y, respectively) to make Cas9-expressing cell lines and documented functional Cas9 activity (Supplemental Figure 1A), using a previously described assay (26). We then transduced negative and positive control sgRNAs into parental, dead Cas9 (dCas9)-expressing, and Cas9-expressing cell lines, and found that growth inhibition was only observed in Cas9-expressing cell lines transduced with positive control sgRNAs, indicating that multiple DSBs are required for growth inhibition (Supplemental Figure 1B).

To test the hypothesis that growth inhibition increased with the number of simultaneously induced DSBs, we transduced the multi-target sgRNAs into Cas9-expressing cells and performed clonogenicity and cell viability assays. The experiment was terminated when non-targeting controls achieved full confluence (1-2 months). We found that in general, clonogenic and cell survival decreased as a function of the number of sgRNA target sites (Figure 1, A and B). Multi-target sgRNAs with 12 target sites or more consistently showed >90% clonogenic inhibition, with

230F(12) demonstrating cytotoxicity similar to that of positive control sgRNAs. We noted variability in this dose-response relationship. For example, the 6- and 7-cutter sgRNAs, 451F(6) and 176R(7), have lower clonogenic inhibition compared to the 5-cutter sgRNA, 715F(5). Statistically significant differences in clonogenic inhibition between cell lines were also detected in cells treated with the 531F(2) sgRNA (Dunn-Sidak test, $P = 0.040$).

We performed γH2A.X staining to quantify CRISPR-Cas9 induced DSBs following transduction with multi-target sgRNAs. We anticipated that targeting the same number of sites with sgRNAs would result in a higher number of γH2A.X foci in TS0111 compared to Panc10.05 since Panc10.05 is hypodiploid with a modal chromosome number of 39-40, whereas TS0111 is hyperdiploid with a modal chromosome number of 50-61. We found that an increased number of sgRNA target sites correlated with an increased number of γH2A.X foci in both cell lines 48 hours post transduction, and that TS0111 cells generally exhibited more foci than the Panc10.05 line (Figure 1, C and D; Supplemental Figure 1C). Transduction of ALU_112a resulted in an excessive number of γH2A.X foci that was uncountable (Supplemental Figure 1D), consistent with the fact that ALU_112a is an Alu element-targeting sgRNA that is expected to generate ~66,533 DSBs per cell (Cas-OFFinder (34)). γH2A.X staining of AGGn (repetitive element-targeting sgRNA) at earlier time points also showed that the number of foci was below saturation before 48 hours (Supplemental Figure 1E). The baseline foci number was ~4 (Figure 1D), consistent with previous literature which established that malignant cells tend to have elevated levels of γH2A.X at baseline (35, 36). Since the number of γH2A.X foci correlated with the number of CRISPR-Cas9 target sites and none of the cells transduced with multi-target sgRNAs showed anomalous foci formation, our data suggest that the clonogenic inhibition by multi-target sgRNAs was a result of targeted DSB induction and not widespread off-target activities.

To ensure that our observations were not limited to constitutive expression of CRISPR-Cas9, we performed electroporation of the CRISPR-Cas9 ribonucleoprotein (RNP) complex into

both cell lines for transient expression. We introduced NT, 230F(12), AGGn, and, for Panc10.05, a combination of 5 sgRNAs targeting 5 different noncoding mutations unique to Panc10.05 and absent in other cell lines (Panc10.05 pool, designed using a novel protospacer adjacent motif (PAM)-based, cancer-specific approach previously described (26); Supplemental Table 2), into cells and performed clonogenic survival assay for 21 days, instead of 1-2 months in our previous assays. Our results were similar to our data in Figure 1 A and B, in which 230F(12) showed >90% clonogenic inhibition (Figure 1, E and F). Differences could be attributed to the confounding effect of cells that did not receive the CRISPR-Cas9 RNP complex and survived. Interestingly, electroporation of 5 Panc10.05-specific sgRNAs (at 1/5 of the concentration used for multi-target sgRNAs) into Panc10.05 cells demonstrated >50% growth inhibition (Figure 1E), showing that transient expression of these mutation-targeting sgRNAs can be growth inhibitory to PC cells.

The cell line-specific sgRNAs target somatic, non-coding mutations in cancer cells that are absent in patient-matched normal cells (26). To study the impact of these cancer-specific sgRNAs on normal cells, we treated two primary skin fibroblasts and two cancer-associated fibroblasts cell lines, all derived from patients, with a pool of 9 sgRNAs specific to either TS0111 or Panc10.05, and cultured for 3-4 weeks to study cell survival (Figure 1G; Supplemental Table 2 and 3). We found no significant differences among the cancer-specific sgRNAs and negative controls, indicating a lack of growth inhibition by these cancer-specific sgRNAs on normal cells which lack these targets.

Simultaneous CRISPR-Cas9 targeting inhibits tumor and metastatic growth

To investigate whether increased number of CRISPR-Cas9 induced DSBs would decrease tumor growth, we first transduced Panc10.05 Cas9-expressing cells with NT, 715F(5), 230F(12), ALU_112a, or the Panc10.05 pool of 9 sgRNAs used in Figure 1G to study impact on normal cells (Supplemental Table 2). After puromycin selection of transduced cells, we injected them

subcutaneously into both flanks of athymic, nude mice, and observed for tumor growth for 6 weeks. The percentage of NT tumors present post xenograft peaked at 90%, followed by 30% of 715F(5) and Panc10.05 pool tumors, and 20% of 230F(12) tumors (Figure 2A). Tumor formation from cells transduced with ALU_112a was not detected (data not shown). Statistically significant decreases in tumor volumes between NT and 230F(12) or Panc10.05 pool were observed as early as week 4 (Figure 1G; Dunn-Sidak test, NT and 230F(12): $P=0.010$, NT and Panc10.05 pool: $P=0.043$, all N=10). By week 6, significant decreases in tumor volumes between NT and the remaining treatment groups were observed (Figure 1G, all $P<0.0001$). Tumors were harvested and weighed by the end of week 6 (Supplemental Figure 2A), which showed significant decreases in tumor weight between NT and the rest of the treatment groups (all $P<0.0001$), but no differences in body weight (Supplemental Figure 2B). To determine whether CRISPR-Cas9 activity had occurred in tumors harvested, we extracted genomic DNA from the two outlier 230F(12) tumors, PCR amplified the 230F(12) target regions, and performed next generation sequencing (NGS). We found that the mutation frequency was 0.97% and 0.64% in 230F(12) tumors, suggesting that the lack of CRISPR-Cas9 activity allowed tumor growth.

Since the primary site of metastasis for PC is the liver, we first established a hemi-spleen injection mouse model of liver metastasis using Cas9-mNeonGreen-expressing Panc10.05 cells (Supplemental Figure 2C). Then, following the method previously described to prepare transduced cells, we transduced NT and 230F(12) sgRNAs and injected these cells into half of the spleen of athymic, nude mice during hemi-splenectomy to seed the liver. 30 days after surgery, livers were harvested, sectioned, and stained with hematoxylin and eosin (H&E) for histology analysis (Figure 2, D and E). While we observed PC metastases in NT-treated livers (Figure 2D; black arrows), tumor regression was detected in the livers of 230F(12)-treated cells (Figure 2E; red arrows), showing that the growth inhibitory effect of multi-targeting by CRISPR-Cas9 can be detected in liver metastases.

We subsequently established a doxycycline-inducible Cas9 (Dox-iCas9) system to examine CRISPR-Cas9 activity in established tumor xenografts. We cloned NT, 230F(12), and L1.4_209F sgRNA sequences into an all-in-one vector, in which doxycycline induces both Cas9 and EGFP, while U6 promoter drives the constitutive expression of a sgRNA (see Supplemental Methods). We transduced Panc10.05 with the cloned vectors, generated derivative cell lines through puromycin selection, and injected them into athymic, nude mice. We also prepared a no-Dox-iCas9, sgRNA-only control ("230F(12) only"), in which no EGFP would be detected in the presence of doxycycline. After tumors were established, we started doxycycline hyclate feed while measuring tumor growth (Supplemental Figure 3A). By the end of week 3, tumors were harvested, weighed, and digested for flow cytometry to detect the presence of EGFP+ cells as an indicator of PC cells (Supplemental Figure 3, B-D). Although we did not detect statistically significant differences in body weights, tumor volumes, and tumor weights among treatment groups (Supplemental Figure 3, A-C), we found significant decreases in PC cells in digested tumors expressing 230F(12) and L1.4_209F compared to NT control (Supplemental Figure 3D; Dunnett's test, NT and 230F(12): *P=0.0005*, NT and L1.4_209F: *P=0.0007*, all N=3). We hypothesized that the lack of phenotypic effect and presence of ~35% EGFP+ cells in tumors treated with 230F(12) and L1.4_209F were due to the incomplete induction of Cas9, as our in vitro correlates (from the same pool of cells used for xenograft) showed a 79.6% induction of Cas9-EGFP in Cas9+NT while treated with doxycycline (Supplemental Figure 3E), suggesting that ~20% of transduced cells were not expressing Cas9. In vitro data also showed reduced growth inhibition of Cas9+230F(12), with 18.5% of living cells expressing EGFP, in contrast with our previous clonogenicity data that showed near complete growth inhibition in 230F(12)-treated cells, indicating that reduced expression of Cas9 and/or sgRNA may be causing tumor growth. Our preliminary data suggests that multi-targeting of CRISPR-Cas9 leads to reduction of cancer cells in established tumors, and further refinement of the Dox-iCas9 model is necessary to observe a meaningful phenotypic effect.

To determine whether CRISPR-Cas9 could be successfully delivered to liver metastases of PC mouse models, we established hemi-spleen injection mouse models of liver metastasis and performed hydrodynamic injection to deliver Firefly luciferase-expressing plasmid to mouse livers (Supplemental Figure 3F). After 72 hours, livers were harvested, digested, and sorted into two cell populations, one for liver cells (Supplemental Figure 3G) and one for PC metastatic cells based on the presence of mNeonGreen fluorescence (Supplemental Figure 3H). Then we stained both cell populations for the presence of Firefly luciferase proteins and performed flow cytometry. While we could not detect the presence of luciferase in the liver cell population (Supplemental Figure 3G), 23.3% of PC metastatic cells expressed luciferase (Supplemental Figure 3H), demonstrating the feasibility of delivering gene therapy to a PC liver metastasis model.

Multi-target sgRNAs exhibit on-target and minimal off-target activities

We subcultured surviving/resistant colonies from clonogenicity assays for another month before extracting genomic DNA to study the targeting activity of the multi-target sgRNAs. Notably, we weren't able to obtain colonies from the 230F(12)- and 676F(16)-treated Panc10.05 cells, and 551R(8)-, 230F(12)-, and 164R(14)-treated TS0111 cells from any of the replicates (Table 1), indicating significant cytotoxicity conferred by these multi-target sgRNAs. We performed whole genome sequencing (WGS) and analyzed the predicted on-target sites and potential off-target sites (Figure 3A). Potential off-target sites with 1-4 base pair mismatches (mm) were predicted by CRISPOR (37) while off-target hits that included gaps were predicted by the Integrated DNA Technologies (IDT) guide RNA design checker (38). Through both manual inspection on the Integrative Genomics Viewer (IGV) and bioinformatics analyses on all potential on- and off-target sites, we found that >95% of mutations came from on-target sites, and only 28% of 1 mm sites were mutated among all of the potential off-target sites (Table 1; Supplemental Data 1). We also failed to detect any mutations at off-target sites containing gaps in Panc10.05 colonies (data not shown).

To further validate these findings, we performed targeted deep sequencing (50,000X coverage) on all the potential 1 mm and 2 mm sites (Figure 3A) and found that only 1 mm sites were mutated but not 2 mm sites (Figure 3, B-C; Supplemental Figure 4, A-B). Our data showed that deep NGS can capture mutations that WGS cannot (Figure 3, B-C), likely due to the limit of detection by WGS at lower (30X) coverage. As an alternative top-down approach to look for potential off-target sites, we identified all novel indels and structural variants (SVs) from WGS data of Panc10.05 surviving colonies and performed homology comparisons between the sequences surrounding the mutations or breakpoints and the sgRNA sequence. None of the sequences surrounding the mutations have fewer than 5 mm compared to the original sgRNA sequence (Supplemental Table 4). We also compared SVs found at non-targeted regions between individual colonies transduced with the same sgRNAs and found that SVs in non-targeted regions were unique to each colony (data not shown). We found one instance of a shared novel SV but the breakpoint differed from the sgRNA sequence by 13 mm, suggesting that it was likely present in the bulk cell line at a low level prior to selection by single-cell cloning.

We then compared the mutation frequencies of the on-target sites in each colony to investigate factors contributing to the variability in clonogenic inhibition (Figure 1A). 451F(6) and 176R(7) sgRNA-resistant colonies showed lower mutation frequency, ~80% and ~36%, respectively, compared to 715F(5) (~97%), suggesting inadequate cutting activity at the 451F(6) and 176R(7) target sites contributing to lower clonogenic inhibition than 715F(5) (Supplemental Figure 4C). 451F(6) sgRNA contains a TT-motif proximal to PAM which could have led to low sgRNA expression when virally expressed (39). Single nucleotide variants (SNVs) were also present in 4 of 6 on-target sites or PAMs of 451F(6) in Panc10.05, further impacting cutting efficiency (Supplemental Data 1). On the other hand, SNVs were found in 4 of 7 in 176R(7) on-target sites in Panc10.05 and 2 of 7 in TS0111, likely contributing to the low overall mutation frequency and clonogenic inhibition (Supplemental Data 1). Moreover, the average on-target

mutation frequencies of 531F(2) sgRNA-resistant colonies were higher in Panc10.05 (100%) than in TS0111 (40%; Supplemental Figure 4C), and the mutation frequencies of 531F(2) 1 mm sites were also higher in Panc10.05 (Figure 3B), suggesting that a combination of decreased on- and off-target activities in TS0111 led to the difference in clonogenic inhibition between Panc10.05 and TS0111.

We quantified the copy number (CN) of each on- and off-target site in the surviving colonies to determine the number of DSBs induced by CRISPR-Cas9. For sgRNAs in which a surviving colony was unavailable, the total number of mutated sites were estimated based on copy number at all on-target sites or assuming mutated sites were the same as the available colony from a different cell line. We found that generally, an increased number of predicted target sites led to an increased number of mutated sites (Supplemental Figure 4D). For Panc10.05, the total copy number of all target sites in 52F(3), 715F(5), and 551R(8) colonies were similar (9-10 cut sites), potentially explaining the similar clonogenic inhibition seen in Figure 1, A and B. The total copy number of all target sites also correlates with the γH2A.X foci data (Supplemental Figure 4E; Pearson r for TS0111 = 0.90, *P=0.038*; Panc10.05 = 0.98, *P=0.003*), suggesting that most of the foci observed were the result of CRISPR-Cas9 induced DSBs.

Simultaneous CRISPR-Cas9 targeting leads to delayed cell death

As an independent measure of growth inhibition, we assessed sgRNA tag survival in the same cell lines on the premise that sgRNAs that are lethal to cells would be eliminated from the pool of sgRNA "tags", while sgRNAs with little to no toxicity would be maintained or enriched. 176R(7) sgRNA was excluded from subsequent analyses due to its low mutation prevalence in surviving colonies (Supplemental Figure 4C). We found that in general, sgRNAs with higher number of target sites demonstrate a greater degree of sgRNA tag loss in Cas9-expressing cell lines but not in parental cell lines (lacking Cas9) 21 days post transduction (Figure 3D; Supplemental

Figure 5A). We compared the sgRNA tag survival results to the results obtained from the clonogenicity assays and found that the data are highly correlated (Spearman r for Panc10.05 = -0.78, $P = 0.001$; TS0111 = -0.92, $P < 0.0001$), suggesting that the sgRNA tag survival assay is a good surrogate for the clonogenicity assay. We also performed sgRNA tag survival on four other PC cell lines and observed a general inverse correlation between the number of sgRNA target sites and sgRNA fold change, showing that the dose-response effect could be observed in a number of PCs despite cell line variations (Supplemental Figure 5B).

Interestingly, most tag reduction of multi-target sgRNAs with high number of cuts did not occur in the first 7 days post-transduction of sgRNAs, but rather between days 7 and 21 (Figure 3E; Supplemental Figure 5, D and F). This was specific to Cas9-expressing cell lines, as parental cell lines transduced with the same sgRNA pool exhibited no obvious difference in sgRNA fold changes across different time points (Supplemental Figure 5, A, C, and E). A comparable experiment by introducing Cas9 through electroporation for transient expression also demonstrated similar observations (Supplemental Figure 5G). To determine whether the temporal delay in tag loss was due to delayed induction of DSBs, we transduced the 164R(14) sgRNA into Panc10.05 Cas9-expressing cells and quantified the mutation frequency at 8 on-target sites over 14 days. We found that scissions and repair occurred over the course of days and peaked at days 3-4 (Figure 3F, R^2 = 0.60-0.74 for all 8 sites), consistent with other published observations (40, 41). Overall, our results indicate that CRISPR-Cas9-induced DSBs are produced within the first few days but do not immediately and directly trigger cell death, pointing to a different mechanism that is contributing to the temporal delay in growth inhibition.

Ongoing and peak CIN induced by CRISPR-Cas9 scissions

To identify chromosomal changes after multiple CRISPR-Cas9 scissions, we performed cytogenetic analyses on cells harvested from 0-21 days post transduction of a multi-target sgRNA

at 3-4 day intervals using a detailed chromosome breakage assay. The TS0111 Cas9-expressing cell line was chosen due to its simpler karyotype than Panc10.05 at baseline (Supplemental Figure 6A). The 164R(14) sgRNA was selected as it had manifested significant growth inhibition in previous dose-response assays. We found that on the first day after transduction of 164R(14), multiple chromosome and chromatid breaks were detected along with radial formations (Figure 4A). Other chromosomal aberrations also accumulated over time, including formation of ring, dicentric, and tricentric chromosomes, telomere-telomere associations, chromosome pulverizations, and endomitosis (Figure 4, A and B; Supplemental Figure 6B). Most of these aberrations peaked at day 14 and decreased by day 21 while chromosome/chromatid breaks remained relatively stable throughout the experiment, showing peak CIN during the ongoing occurrence of breakage events (Figure 4, A and B). We also analyzed breakpoints of dicentric, tricentric, and ring chromosomes to determine whether they occurred at CRISPR-Cas9 targeted or non-targeted regions. Although SVs at targeted regions predominated at early time points and decreased over time, the majority of SVs occurred at non-targeted regions and peaked at day 14 (Figure 4C), consistent with ongoing chromosomal rearrangements. While most targeted regions were located at telomeric regions, 61.5% of novel SVs identified at non-targeted regions were also located at telomeric regions (Supplemental Figure 6C). To investigate whether SVs found at targeted regions were direct results of CRISPR-Cas9 targeting, we performed a break-apart fluorescence in situ hybridization (FISH) assay at one of the 164R(14) sgRNA target sites (Figure 4, D-F). While simple rearrangements were observed at early time points (Figure 4E), more complex rearrangements were observed at later time points (Figure 4F). The number of cells with abnormal FISH patterns increased over time and peaked at day 14 (Figure 4D), demonstrating ongoing chromosomal rearrangements that originated from the initial CRISPR-Cas9 scissions.

TS0111 cells also responded to the 164R(14) sgRNA by becoming polyploid, manifesting as extremely large nuclei or multinucleated giant cells, with cells containing >100 chromosomes

detected by cytogenetic analyses (Figure 5A; Supplemental Figure 6, D and E). An X/Y FISH assay, used to count cells with multiple (>6) X chromosomes, showed that polyploidy peaked at day 10 and decreased by day 21 (Figure 5B). Additionally, we assayed apoptosis markers in cells transduced with 164R(14) to determine if apoptosis was involved in the cell death mechanism. We found that the proportion of apoptotic cells stained with annexin V increased on days 7 and 14 compared to cells transduced with a non-targeting sgRNA, and decreased by day 21 (Figure 5C). We were consistently unable to harvest enough living cells for flow cytometry analyses on day 21. TUNEL (terminal deoxynucleotidyl transferase dUTP nick end labeling) assay, on the other hand, was used to detect late stages of apoptosis and showed increased signal on day 21 (Supplemental Figure 6F).

We also analyzed the surviving colonies from our clonogenicity assays using WGS to identify, categorize, and quantify novel SVs. This approach would allow us to study the effect of DSB repair at both targeted and non-targeted regions at high resolution. We used the SV detection software, manta (42), to identify SVs in surviving/resistant colonies previously transduced with multi-target sgRNAs, followed by visual inspection of all identified SVs using IGV. Our data show that while CRISPR-Cas9 induced SVs (1- and 2-target SVs) increased as a function of the number of sgRNA target sites, most of the SVs detected (87%) were novel SVs arising from endogenous DSBs (0-target SVs), which increased and peaked at 451F(6) sgRNA-resistant colonies, followed by a decrease in SVs in 551R(8)- and 164R(14)-resistant colonies (Figure 5, D and E). Notably, translocations increased as a function of the number of sgRNA target sites (Figure 5F). We also analyzed the sequences at breakpoint junctions for indels and microhomology (Figure 5G), which could indicate involvement of non-homologous end joining (NHEJ), microhomology-mediated end joining (MMEJ), and single-strand annealing (SSA) (43, 44). We found that multi-target sgRNA transduced cells presented with a higher proportion of breakpoints that involved 1-20bp microhomologies compared to non-targeting control (Supplemental Figure 6G; Supplemental Table

5), indicative of the involvement of MMEJ in the repair of the DSBs. Overall, both cytogenetics and WGS analyses reveal that CRISPR-Cas9 scissions lead to continuous generation of novel chromosomal rearrangements which peak at a tolerable limit, suggesting that CRISPR-Cas9-induced extreme CIN that is not conducive for cell survival.

CRISPR-Cas9-induced DSBs cause higher cytotoxicity than irradiation

This CRISPR-Cas9-induced CIN showed similarities to observations reported from irradiation (IR) studies, in which delayed manifestations of CIN and cell death are observed over several generations after IR (45–47). We sought to compare the cytotoxicity between CRISPR-Cas9-induced DSBs and IR-induced DSBs to investigate differential effects on cancer cell growth. First, we determined the number of DSBs induced by irradiating Panc10.05 and TS0111 with 0-10 Gy and performed γH2A.X staining. Our data demonstrated a dose-response induction of DSBs (Figure 6, A and B; Supplemental Figure 7A), and cells treated with 4Gy and above showed excessive number of foci that were uncountable (data not shown).

To compare the effect of IR-induced versus CRISPR-Cas9-induced DSBs on cell survival, we determined clonogenic inhibition in Panc10.05 and TS0111 cells following IR or multi-target sgRNA transduction. Clonogenic inhibition increased as a function of both IR dose and sgRNA target sites 21 days post treatment (Figure 6C). Notably, 715F(5) sgRNA induced similar clonogenic inhibition as 2Gy IR (~55% and ~56%, respectively). >90% clonogenic inhibition was observed after 4Gy in TS0111 and 6Gy in Panc10.05, while >98% clonogenic inhibition was observed in 230F(12) sgRNA-treated cells from both cell lines. Cell viability assays corroborated our clonogenicity findings (Supplemental Figure 7, B and C). We also quantified cell survival by counting IR-treated cells every 3-4 days over 21 days, and confirmed that increased IR dose decreased cell number, in which TS0111 demonstrated higher sensitivity to IR than Panc10.05 (Supplemental Figure 7, D and E).

We graphed clonogenic survival as a function of γH2A.X foci, and discovered that a much smaller number of DSBs induced by CRISPR-Cas9 compared to IR was sufficient to yield similar levels of clonogenic inhibition (Figure 6D). For example, although 715F(5) sgRNA and 2Gy IR lead to a similar reduction in clonogenic survival, the number of γH2A.X foci detected in 715F(5) sgRNA-treated cells (~11 foci) was much lower than that of 2Gy treated cells (~36 foci). Radiation doses of 4-10Gy were highly toxic to both cell lines, resulting in an almost complete loss of survival while inducing an excessive number of foci that were uncountable. Notably, we observed the same amount of growth inhibition in 230F(12)- and 164R(14)-treated cells that displayed a much lower amount of γH2A.X foci compared to equitoxic radiation doses. Our data indicates that CRISPR-Cas9-induced DSBs are significantly more cytotoxic than a similar amount of IR-induced DSBs.

Since we have discovered that the cytotoxicity from CRISPR-Cas9-induced DSBs stemmed from the induction of ongoing chromosomal rearrangements, we hypothesized that the lower cytotoxicity from IR-induced DSBs could be due to transient DSB formation followed by immediate repair as opposed to persistent DSBs induced by CRISPR-Cas9 scissions. We electroporated in CRISPR-Cas9 RNP complex containing 230F(12) sgRNAs into both PC cell lines, quantified their γH2A.X foci across various timepoints, and compared them to cells treated with 1Gy (Figure 6, E-G; Supplemental Figure 8). As electroporated cells were not fully attached prior to the 16-hour (h) timepoint, we did not include data before 16h to avoid potential confounding effects. Our data showed that 230F(12) sgRNA treatment led to formation of persistent γH2A.X foci up until our final timepoint (day 7), with foci expression peaking and plateauing starting at 16h (Figure 6, E and F; Supplemental Figure 8A). High variability could be seen in Panc10.05, potentially due to presence of cells that did not receive the CRISPR-Cas9 RNP complex and survived. Meanwhile, γH2A.X expression of irradiated cells peaked at 15 minutes and decreased over time, with foci number similar to baseline at 48h (Figure 6, E and G; Supplemental Figure 8B), reflecting a completion of DSB repair within that time period. To ensure that electroporation

alone did not increase γH2A.X expression, we introduced a non-targeting sgRNA (NT) and counted foci at 48h, which revealed an average of 5.9 foci upon counting 100 cells, consistent with our baseline data. Together, our data indicate that while IR-induced DSBs are rapidly repaired, CRISPR-Cas9-induced DSBs persist for a prolonged period of time.

Cells resistant to one sgRNA retain sensitivity to other sgRNAs and do not significantly augment disease

To investigate whether the surviving/resistant colonies from the clonogenicity experiment (Figure 1A) might increase tumor growth compared to non-transduced cells, we first checked for mutations at the multi-target sgRNA target sites of each colony using deep NGS to confirm their resistance against CRISPR-Cas9-induced DSBs (Figure 7A). We found that the overall mutation frequency of all target sites in each colony was >99%, confirming that these colonies had their target sites mutated during the first round of sgRNA transduction. Then, we injected parental and resistant cells into athymic, nude mice subcutaneously and observed tumor growth over 33 days (Figure 7B). We noticed decreased tumor growth in one of the two non-targeting controls (NT #1) and 715F(5)-resistant tumors (715F(5)), and no significant differences with other resistant tumors compared to the parental/non-transduced control (NTC). We harvested tumors 33 days post xenograft or postmortem (Supplemental Figure 9A) to measure their weights, and found generally no significant differences between resistant tumors and non-transduced controls, except for 715F(5)-resistant tumors that showed decreased weight (Figure 7C). No difference in body weight was noted as well (Figure 7D). Thus, we found that DSB-resistant cells induced by CRISPR-Cas9 do not grow significantly faster than the non-transduced or the NT-transduced cells in subcutaneous xenograft mouse models.

Finally, we hypothesized cells that survived the initial set of CRISPR-Cas9-induced DSBs could be eliminated by a new set of CRISPR-Cas9-induced DSBs. Using surviving colonies from

our clonogenicity assay with a subset of their target sites validated for mutations using NGS (Supplemental Figure 9B), we re-transduced these colonies with the non-targeting sgRNA (NT2), multi-target sgRNA that was already expressed in the colonies (e.g. 715F(5)-resistant colonies were treated with 715F(5) sgRNA), 230F(12), and 164R(14) sgRNAs. We found that after 21 days, in the colonies that we had tested, no growth inhibition was observed in cells treated with the non-targeting control nor those re-transduced with their original sgRNAs, but found >96% inhibition with 230F(12) sgRNA and >87% with 164R(14) sgRNA (Figure 7, E and F; Supplemental Figure 9C). We collected double-resistant colonies (i.e. cells that survived the original transduction and the secondary transduction) and performed NGS on their target sites. For 230F(12)-resistant colonies, the 230F(12) target sites were not mutated (Supplemental Figure 9D), suggesting that CRISPR-Cas9 activity from the secondary transduction was absent in the double-resistant colonies. We detected ~38% mutation frequency with colonies transduced with 164R(14) sgRNA (Supplemental Figure 9D), suggesting that the majority of cells that survived lacked CRISPR-Cas9 activity from the secondary transduction.

Discussion

In our study, we show that simultaneous induction of multiple CRISPR-Cas9-induced DSBs overwhelm the integrity of the DSB repair system to repair the DNA breaks correctly, leading to extreme CIN and cell death. We designate this phenomenon as “chromosome catastrophe” because the simultaneous DSBs initiate a chromosome-level process of karyotypic aberrations and polyploidization that results in cell death. This is elucidated especially in our rare surviving colonies, which show that the vast majority of SVs did not result from direct CRISPR-Cas9 targeting, but rather resulted from the catastrophic process initiated from the original set of simultaneous CRISPR-Cas9-induced DSBs.

Additionally, we reveal that CRISPR-Cas9-induced DSBs are significantly more toxic than a similar number of IR-induced DSBs, with persistent DSBs demonstrated in sgRNA-treated cells compared to transient DSBs in IR-treated cells. This is likely due to multiple repeated cycles of DSB induction at CRISPR-Cas9 target sites before NHEJ-mediated errors alter the sgRNA-recognition sequence, thus preventing further DNA cleavage (48). Repeated cycles of DNA cleavage and repair have been previously observed with endonuclease-based systems unless the endonuclease activity was specifically turned off (49, 50). In contrast, DSBs are induced by IR in a single pulse followed by immediate repair. The γH2A.X foci count in multi-target sgRNA-transduced cells could be an underestimation, as the number of DSBs detected in WGS (by quantifying the copy number of mutated sites) tends to be higher; e.g. 12 foci/DSBs were detected from γH2A.X staining in TS0111 715F(5)-treated cells, while 16 DSBs were detected in WGS. However, if we consider both background DSB formation (~4 foci) and DSBs from CRISPR-Cas9 as detected by WGS, the number of CRISPR-Cas9-induced DSBs in sgRNA-treated cells are still lower than that of IR. Consequently, targeting 6-8 genomic sites with CRISPR-Cas9 results in similar cancer cell kill as 2Gy IR. Our results highlight the therapeutic potential of CRISPR-Cas9 based on its ability to induce tumor cell death similar to clinically relevant doses of radiation (51). Future experiments will combine CRISPR-Cas9-induced DSBs with current chemotherapies that induce CIN, such as paclitaxel, or other agents that induce CIN selectively, such as KIF18A inhibitors, to enhance the elimination of cancer cells (52–55).

Based on our sgRNA design strategy, most of our multi-target sgRNA target sites are located near telomeres, possibly contributing to the cell death observed. Multi-target sgRNA treated cells exhibited similar CIN features to those observed in cells undergoing telomere crisis, such as massive chromosomal rearrangements and endoreduplication, which result in a high rate of cell death (56, 57). Umbreit and colleagues (2020) also demonstrated the generation of chromosome bridges by using CRISPR-Cas9 to target chr4 subtelomere of telomerase-immortalized RPE-1 cells,

supporting the idea of targeting telomeric regions to generate CIN (19). We found that microhomologies were involved in the majority of breakpoints found in multi-target sgRNA-transduced colonies, consistent with existing literature suggesting that MMEJ is a major player in CRISPR-Cas9 induced DSB repair (58–60). A potential avenue could be comparing the cytotoxicity between near-telomeric and near-centromeric targeting, and whether the cytotoxicity could be enhanced with an MMEJ inhibitor.

Additionally, polyploidization of cancer cells has been associated with therapeutic resistance and tumor repopulation, as it enables more phenotypic variation compared to non-polyploid cells (61–63). However, this does not explain why we could not obtain surviving colonies from cells treated by some of our multi-target sgRNAs that had been grown for about three months after transduction. We also did not observe significant polyploidization by Cas9-expressing cells alone or cells treated with non-targeting sgRNAs, suggesting that Cas9 or sgRNA expression itself does not cause polyploidization of cancer cells. As both damaged telomeres and polyploidy have been associated with increased risk of chromothripsis (64, 65), we suspect that the polyploidization of multi-target sgRNA treated cells allowed more CIN that led to lethal consequences instead of providing a permissive background for tumorigenicity. We also found very few SVs at the CRISPR-Cas9 on-target sites in our surviving colonies, though we observed CRISPR-Cas9-induced rearrangements in our break-apart FISH assay, suggesting that the surviving colonies might have lower levels of CIN compared to the rest of the non-surviving cells. Future studies should examine whether the surviving colonies obtained were progenies of polyploid cells, and whether they were outliers in terms of CIN rate compared to the rest of the cell population.

We also found significant advantages of integrating conventional chromosome analysis with WGS while studying CIN for a few reasons: (1) cytogenetics analyses are more likely to reflect the “truth,” as chromosomes are directly, visually inspected for the presence of breakpoints and chromosomal aberrations, while SV-calling software could be affected by various artifacts such as

mapping errors at the repetitive regions (66); (2) WGS analyses can pinpoint the nucleotide sequence of breakpoints and allow us to examine for potential off-target activity at a much higher resolution than cytogenetics analyses; (3) cytogenetic analyses allowed us to witness the formation of chromosomal aberrations that are known to directly contribute to CIN due to mitotic errors, while WGS analyses heavily rely on the parameter settings to accurately call out structural abnormalities; (4) WGS analyses can capture smaller variations such as small indels and single nucleotide variants, features that are overlooked by cytogenetics approaches due to detection resolution. Although significant progress has been made to improve SV callers, cytogenetics analyses remain valuable to provide whole-genome data of major genomic rearrangements at a single cell level.

While the copy number of individual genomic sites were measured based on WGS from the Cas9-derived cell line prior to CRISPR-Cas9 treatment, we acknowledge that the surviving clones that stemmed from our CRISPR-Cas9 treatment might have their own aneuploid distribution due to genomic instability and subclonality. Since our WGS analyses were performed on two surviving clones for each treatment, our results were expected to overcome the background variability inherent to individual subclones. We will remain cognizant that subclones exist within malignant tumors and vary from the bulk of the cancer in a clinical setting. In this regard, we studied multiple metastases in five patients from a rapid autopsy study and identified regions of truncal loss-of-homozygosity that were consistently present across metastases, despite some overall genomic instability (67).

We demonstrate cells that survived CRISPR-Cas9 scission did not contribute to higher tumor growth rate, likely because the scissions were not induced in tumor suppressor genes. Notably, we show that cells that survived the initial round of CRISPR-Cas9 scissions could still be eliminated by a second round of CRISPR-Cas9 scissions at different genomic locations. This has major clinical implications, as it suggests that cancer cells do not develop resistance against CRISPR-Cas9-induced DSBs and are susceptible to continuous rounds of DSBs for cell killing.

This highlights the potential of CRISPR-Cas9 as a novel targeted therapy that does not target a specific oncogenic pathway but is solely based on the induction of multiple DSBs to eliminate cancer cells.

Targeting cancer in vivo will require successful delivery. Viral delivery is common in gene therapy, but this modality carries significant limitations and risks (e.g. immunogenicity, packaging capacity, complex production, regulatory and safety concerns) (68–70). Nanoparticles, particularly lipid nanoparticles (LNPs) that encapsulate Cas9 mRNA along with therapeutic sgRNAs, have shown promising efficacy and safety in patients in early phase clinical trials (71–73). While our safety data indicated that delivery to normal cells should be well-tolerated, we will likely require additional moieties to provide preferential delivery to the cancer cells being targeted (74, 75). Moreover, virus-like particles and exosome-based strategies are emerging delivery platforms for gene therapy (76, 77), and more clinical data will be needed to assess their therapeutic potentials. As LNP delivery to liver is well established and liver is a common site of metastatic spread for various cancers (e.g. breast, colorectal, pancreatic, lung, melanoma) (78), our first clinical setting for initial trials could be to treat liver metastases.

In summary, we establish that a small number of CRISPR-Cas9-induced DSBs at non-coding regions could lead to PC cell death, and this cytotoxicity, which is more potent than IR, is driven by an accumulation of CIN events that leads to chromosome catastrophe. We also show that by using sgRNAs that are specific to a patient's cancer, we could achieve tumor growth inhibition. As novel therapies are urgently needed for PC patients, this study highlights the potential of CRISPR-Cas9 as a novel and selective cell killing strategy against PC.

Methods

Clonogenicity and cell viability assays

For transduction of multitarget sgRNAs, cells were transduced with lentivirus carrying sgRNA-expressing plasmids at MOI 10 into media containing 10ug/mL polybrene. Cell culture conditions were described in Supplemental Methods. After 20h of incubation, cells were washed once with 1X PBS and incubated in normal media. Next day, cells were split into 96-well plates in 1:1000 dilution for clonogenic survival under 1ug/mL puromycin or 200ug/mL hygromycin selection. For electroporation of CRISPR-Cas9 RNP complex (electroporation protocol described in Supplemental Methods), electroporated cells were evenly plated on 96-well plates for clonogenic growth. For transduction of normal cell lines, MOI was increased to 50 and cells were plated on 96-well plates containing 500 cells/well. Negative controls consisted of equivalent doses of NT and NT2 sgRNAs, while positive controls consisted of equivalent doses of AGGn, L1.4_209F, and ALU_112a sgRNAs. For radiation, cells were treated with 0-10 Gy of radiation (CIXD X-RAY irradiator, xstrahl) and split into 96-well plates in 1:1000 and 1:10,000 dilutions on the same day. For all experiments, at the specified endpoint described in Results or figure legends, colony counting was performed using phase microscopy and alamarBlue Cell Viability Reagent (ThermoFisher) was added according to manufacturer's instructions. Fluorescence reading was performed on BMG POLARstar Optima microplate reader to assess cell viability. Excitation was set at 544nm and emission at 590nm, with a gain of 1000 and required value of 90%.

γH2A.X staining and imaging

Cells were seeded at a density of $2x10^5$ cells/well of a 6-well plate with coverslips. For transduction of multitarget sgRNAs, cells were transduced and washed as described above. 48h post-transduction or at predetermined timepoints post-electroporation, cells were fixed. For the

radiation experiment, cells were treated with the indicated doses of radiation (CIXD X-RAY irradiator, xstrahl) and fixed at predetermined timepoints post radiation. For both experiments, cells were fixed with 4% paraformaldehyde for 20mins at room temperature. Cells were then washed twice with 1X PBS for 5mins each, blocked and permeabilized with 5% BSA / 0.5% Triton X-100 in PBS for 30mins at room temperature, followed by an overnight incubation with anti-phospho-Histone H2A.X (Ser139) antibody (# 05-636, Sigma Aldrich) at 1:1000 dilution. Next day, cells were washed thrice with PBS for 5mins each and subsequently incubated with secondary antibody conjugated with Alexa Fluor 594 (# A-11032, ThermoFisher Scientific) for 1hr at room temperature. Cells were again washed thrice with PBS and then counterstained with DAPI containing mounting medium (# H-1800, Vector Labs). Stained cells were imaged using a fluorescence microscope (Zeiss AxioImager Z1) with a 40X objective. γH2A.X foci were counted manually under the microscope with a minimum of 100 nuclei for each sample.

Mouse experiments and sex as a biological variable

Protocols to make the Cas9-expressing cell line for xenograft and xenograft-adapted parental cell line are available in Supplemental Methods. All mouse experiments were double-blind studies and used only female mice for practical reasons (e.g. less fighting).

For the subcutaneous xenograft mouse experiment using pre-treated cells, Cas9-expressing Panc10.05 cells were transduced with lentivirus containing sgRNA-expressing plasmids at MOI 10. Cells were puromycin-selected for 7 days, then injected into female, 12-week old nude, athymic mice (Envigo). Prior to xenograft, mice were randomized by weight and housing to consist of 5 mice per treatment group. $5x10^5$ cells per tumor in 100uL PBS were subcutaneously implanted into the right and left flanks, with each mouse bearing two tumors. Body weight and tumor volume were measured weekly by an investigator who was blinded by the treatment groups. Mice were also

monitored for adverse effects. 6 weeks post xenograft, tumors were surgically extracted and weighed by two investigators who were blinded by the treatment groups.

For experiments involving hemi-spleen injection mouse models for PC liver metastasis, cells were pre-treated as described previously. Female, 8-week old nude, athymic mice (Envigo) were randomized by weight and housing to consist of 5-7 mice per treatment group. After a week of puromycin selection, mice underwent a hemi-splenectomy where $1x10^6$ cells were injected in half of the spleen per mouse to seed the liver. Surgeries were completed in a surgical suite with autoclaved surgical tools and a sterile drape covering the surface of the warming table. Mice were anesthetized in a chamber using isoflurane (2 L/min O2, 2% Isoflurane) for 5 minutes. Anesthetized mice were transferred to a surgical platform affixed with tubing to maintain anesthetized state. Lubricant was added to each eye to avoid drying. Mice were laid on their right side with their left flank facing up towards the surgeon. Mice were wiped unidirectionally with an ethanol wipe 3 times. Toe pinch was administered to ensure mice were at optimal anesthetic depth. Scissors and forceps were used to gently lift the skin and make a 1 cm linear incision in the dermis and peritoneal cavity. Forceps were used to gently lift and expose the spleen. Two titanium ligating clips were placed near the center of the spleen. Using scissors, the spleen was cut in half between the two ligating clips. The anterior half was placed back into the peritoneal cavity. Using a 1-mL TB syringe with a 25-gauge needle, 50uL of PBS were aspirated followed by 100uL of tumor cell suspension in DMEM tissue culture media. The final volume of 150uL was injected into the posterior half of the spleen slowly. After several seconds, two titanium ligating clip were used to clamp the vessels descending from the posterior half of the spleen. The posterior half of the spleen was then removed. A 4-0 absorbable silk suture was used to create a continuous double stitch in the mucosa layer followed by 2 discrete sutures to close the incision in the skin. Finally, a surgical clamp was used to secure the incision further. Following surgery, mice were placed in a clean cage on a warming table and monitored for 30 minutes. Mice were assessed daily for signs of discomfort following

surgery. Livers were harvested from mice 30 days after hemi-splenectomy. The left lobes of each liver were placed in a cassette and fixed in 10% formalin at room temperature for 48 hours. After fixing, livers were paraffin embedded. For each liver, 5um tissue sections were collected at 250-um levels between each section, yielding approximately 10 slides per liver. Tissue sections were H&E stained and evaluated by a liver pathologist for abnormal tissue features.

Protocol for Dox-iCas9 mouse experiment can be found in Supplemental Methods. For the hydrodynamic injection experiment, the establishment of a hemi-spleen injection model was the same as previously described. The hydrodynamic injection protocol and luciferase protein detection was detailed in Supplemental Methods.

For the experiment with surviving colonies, cells were cultured under blasticidin and puromycin selection to maintain Cas9 and sgRNA expressions, then injected into female, 6-week old nude, athymic mice (Envigo). Prior to xenograft, mice were randomized by weight and housing to consist of 5 mice per treatment group. $5x10^6$ cells per tumor in 50uL matrigel (Corning) were subcutaneously implanted into the right and left flanks, with each mouse bearing two tumors. Body weight and tumor volume measurements were collected weekly by an investigator who was blinded by the treatment groups. Mice were also monitored for adverse effects. 5 weeks post xenograft, tumors were surgically extracted for weighing by two investigators who were blinded by the treatment groups.

Cut site determination and off-target analysis from WGS data

WGS of surviving colonies was described in Supplementary Methods. BAM files were put into Integrated Genome Viewer (IGV (79)) to inspect all perfect and potential off-target sites (up to 4 mm). Actual cut site was determined by presence of mutation (insertion, deletion, or structural variant) at the sgRNA target region. Quantification of mutation frequency of all target sites was done using CRISPRessoWGS (80). For mutations that were SVs, quantification was manually done

on IGV. All predicted 1 mm and 2 mm sites in each colony were analyzed by PCR and deep sequencing to verify and quantify mutations (Supplementary Methods). As an alternative approach to look for off-target activity, MuTect2 v3.6.0 (81) was used to call somatic variants between the sample-control pairs. The default parameters and SnpEff (v4.1) (82) were used to annotate the passed variant calls. Manta v0.29.6 (42) was used to call somatic SVs and indels between the sample-control pairs. The default parameters were used. Variants were annotated according to UCSC refseq annotations using an in-house script. From the list of results generated, we looked for loci within the Excel files that closely matched our sgRNA sequence. This was performed with an R script that performed the following steps: 1) Read in an Excel file containing one mutation per row. 2) Obtain the forward and reverse strand sequences from the hg19 genome between the start – 50 bp and stop + 50 bp positions of the locus. 3) Align each locus's forward and reverse sequences to the target sgRNA with no gaps using the Smith-Waterman algorithm. 4) Determine the number of mismatches between the sgRNA and the nearest matching piece of DNA within each junctions. 5) Output the original information along with new columns displaying the mismatches between each junction and the sgRNA into a new Excel file. From the list of outputs, we only consider potential target sites that have <5bp mismatches to the sgRNA sequence.

sgRNA tag survival assay

Cells were transduced with a lentivirus pool containing all the sgRNAs in table S1 at MOI 0.1 into media containing 10ug/mL polybrene. After 24h, approximately 1 million cells were collected for day 1 timepoint, and the remaining cells were cultured for another day then subjected to 1ug/mL puromycin selection. Cells were collected on days 1, 7, 14, and 21 post-transduction and gDNA extractions were performed using QIAamp UCP DNA Micro Kit (QIAGEN) by following the manufacturer's protocol. sgRNA library was prepared by amplifying the sgRNA target region from gDNAs using next generation sequencing (NGS) primers provided by Joung et al. (83), based

on the protocol outlined in the paper, and sent for NGS (Primers Table 1). Read counts of each sgRNA were extracted from FASTQ files using the script provided by Joung et al. (83) and were put through the MAGeCK (84) pipeline to obtain sgRNA fold change.

Chromosome breakage assay

TS0111-Cas9-EGFP cells plated at 5×10^5 /ml were treated with 164R(14) sgRNA and harvested at 0, 1, 3, 7, 10, 14, 16 and 21 days. Colcemid (0.01 μg/ml) was added 20h before harvesting. Cells were then exposed to 0.075 M KCl hypotonic solution for 30mins, fixed in 3:1 methanol:acetic acid, and stained with Leishman's for 3 mins. For each treatment, 100 consecutive analyzable metaphases were analyzed for induction of chromosome abnormalities including chromosome/chromatid breaks and exchanges.

1q41 Break-apart FISH assay

FISH was performed on the TS0111-Cas9-EGFP cells before and after 164R(14) sgRNA treatment (0, 1, 3, 7, 10, 14, 16 and 21 days) using RP11-14B15 and RP11-120E23 probes flanking a 1q41 sgRNA cut according to the manufacturer's protocol (Empire Genomics Inc., Williamsville, NY). The RP11-14B15 probe binds the 5' (centromeric) side of the 1q41 sgRNA cut and in Spectrum Orange. The RP11-120E23 probe binds the 3' (telomeric) side of the 1q41 sgRNA cut and in Spectrum Green. For these probes, an overlapping red/green or fused yellow signal represents the normal pattern, and separate red and green signals indicate the presence of a rearrangement. The normal cutoff was calculated based on the scoring of the TS0111-Cas9-EGFP cells before sgRNA treatment (day 0). The normal cutoff for an analysis of 500 cells with the 1q41 break-apart probe set is calculated using the Microsoft Excel β inverse function, = BETAINV (confidence level, false-positive cells plus 1, number of cells analyzed). This formula calculates a one-sided upper confidence limit for a specified percentage proportion based on an exact

computation for a binomial distribution assessment. The normal cutoff for the 1q41 break-apart probe set is 0.6% (for a 95% confidence level). For each time point, a total of 500 nuclei were visually evaluated with fluorescence microscopy using a Zeiss Axioplan 2, with MetaSystems imaging software (MetaSystems, Medford, MA), to determine percentages of abnormal cells.

X/Y FISH assay

FISH was performed on the TS0111-Cas9-EGFP cells before and after a 164R(14) sgRNA treatment (0, 1, 3, 7, 10, 14, 16 and 21 days) using X/Y centromere FISH probes according to the manufacturer's protocol (Abbott Molecular Inc., Des Plaines, IL). For each time point, a total of 200 nuclei were visually evaluated with fluorescence microscopy using a Zeiss Axioplan 2, with MetaSystems imaging software (MetaSystems, Medford, MA), to determine copy number of the X chromosome. The specimen was considered abnormal if the results exceeded the laboratory-established cutoff for the X/Y probe set.

SV identification and quantification

From the WGS BAM files of surviving colonies, Manta v0.29.6 was used to call somatic SVs between the sample and the control, in which the control is the Panc10.05-Cas9-EGFP non-transduced cell line. The default parameters were used. Variants were annotated according to UCSC refseq annotations using an in-house script. The list of SVs generated were then individually, visually inspected on IGV to validate its presence in sample and absence in control. Novel SVs that have passed the manual screening were quantified and characterized. Breakpoint junctions were also analyzed for microhomology manually.

Statistical analysis

The appropriate statistical tests were performed in GraphPad Prism (Version 9.2.0). The statistical models used were stated in results and figure legends. For all statistically significant results, * indicates $P<0.05$, ** indicates $P<0.01$, *** indicates $P<0.001$, and **** indicates $P<0.0001$.

Study approval

Mouse experiments were approved by the Johns Hopkins University Animal Care and Use Committee (MO24M222). Cell line collections and uses from patient samples were approved by The Johns Hopkins Medicine Institutional Review Boards (NA_00074387).

Data availability

The authors confirm that the data supporting the findings of this study are available within the article and its supplementary material when possible. Plasmids constructed had been deposited at Addgene. Plasmids expressing various specific sgRNAs are available upon request from JRE. Regarding cell lines, except for Panc10.05 which is an ATCC line, the rest of the cell lines and their derivative cell lines (including Panc10.05-derived lines) are available via Material Transfer Agreements. Values for all data points in graphs are reported in the Supporting Data Values file. The authors declare that the sequencing data for this study cannot be shared publicly due to IRB restriction on sharing de-identified data that aligns with the consent of research participants. Researchers can request more detailed data from the corresponding author shared though an approved collaboration arrangement.

AUTHOR CONTRIBUTIONS

SSKT, AK, AB, NJR, MG, YSZ, and JRE conceived of and designed the study. SSKT, AK, AB, EHS, LM, and QZ conducted experiments. SZ, YS, AS, KB, HL, CFH, and RAA contributed to the acquisitions and analyses of data. CFH, RAA, NJR, RBS, MG, YSZ, and JRE provided resources and supervision. SSKT and JRE wrote the original draft of the manuscript. SSKT, AK, AB, EHS, LM, KB, RHH, CFH, RAA NJR, RBS, MG, YSZ, and JRE provided critical revisions to the manuscript. The authorship order among the co-first authors was determined to reflect their substantial contribution to the study, while acknowledging varying degrees of involvement in the collaborative work.

ACKNOWLEDGEMENTS

We would like to acknowledge Drs. Michael Goggins, Hai-Quan Mao, Sarah Wheelan, Ming-Tseh Lin, Lei Zheng, Elizabeth M. Jaffee, Feyruz V. Rassool, Richard Burkhart, Christine Iacobuzio-Donahue, Jessica Gucwa, Shiwen Peng, Minh-Tam Pham, Alok Mishra, and Aparna Pallavajjala for helpful discussions. We thank Ada Tam, Raluca Yonescu, Emily Adams, Lisa Haley, Anuj Gupta, Celinia Ondeck, Jingyao Ma, Yining Zhu, Jacqueline Tang, Fidel Cai, Lee Blosser, and Victoria Stinnett for outstanding technical assistance.

Funding:

National Institutes of Health grant R21CA164592 (JRE)

National Institutes of Health grant P50CA62924 (SKCCC)

National Cancer Institute CCSG P30CA006973 (SKCCC)

The Sol Goldman Pancreatic Cancer Research Center (JRE)

PanCan/AACR Innovation Award (JRE)

The STRINGER Foundation (JRE)

Casimir H. Zgonina Family Endowment for Pancreatic Cancer Research (JRE)

Dennis Troper and Susan Wojcicki (JRE)

Dick Knox/Cliff Minor Fund (JRE)

Edward A. Goldsmith Pancreatic Cancer Research Fund (JRE)

Elaine Crispen Sawyer Endowment (JRE)

Elaine T. Koehler Pancreatic Cancer Research Fund (JRE)

Eve Stancik Memorial Fund (JRE)

George Rubis Endowment for Pancreatic Cancer Research (JRE)

Hilda Buchfeller Yost Young Investigator's Fund (JRE)

James S. McFarland Endowment for Pancreatic Cancer Research (JRE)

John J. Lussier Pancreatic Cancer Research Fund (JRE)

Linda C. Talecki Gallbladder Cancer Research Fund (JRE)

Mary M. Graf Memorial Endowment Fund for Gallbladder Cancer (JRE)

Mary Lou Wootton Endowment (JRE)

Professor J. Mayo Greenberg and Dr. Samuel L. Slovin Endowment (JRE)

Rawlings Family Pancreatic Cancer Research Fund (JRE)

REFERENCES

1. Sansregret L, Vanhaesebroeck B, Swanton C. Determinants and clinical implications of chromosomal instability in cancer. *Nat Rev Clin Oncol*. 2018;15(3):139–150.

2. Sotillo R, et al. Mad2-induced chromosome instability leads to lung tumour relapse after oncogene withdrawal. *Nature*. 2010;464(7287):436–440.

3. Rowald K, et al. Negative Selection and Chromosome Instability Induced by Mad2 Overexpression Delay Breast Cancer but Facilitate Oncogene-Independent Outgrowth. *Cell Rep*. 2016;15(12):2679–2691.

4. Birkbak NJ, et al. Paradoxical relationship between chromosomal instability and survival outcome in cancer. *Cancer Res*. 2011;71(10):3447–3452.

5. Roylance R, et al. Relationship of extreme chromosomal instability with long-term survival in a retrospective analysis of primary breast cancer. *Cancer Epidemiol Biomarkers Prev*. 2011;20(10):2183–2194.

6. Silk AD, et al. Chromosome missegregation rate predicts whether aneuploidy will promote or suppress tumors. *Proc Natl Acad Sci U S A*. 2013;110(44):E4134–41.

7. Janssen A, Kops GJPL, Medema RH. Elevating the frequency of chromosome mis-segregation as a strategy to kill tumor cells. *Proc Natl Acad Sci U S A*. 2009;106(45):19108–19113.

8. Godek KM, et al. Chromosomal Instability Affects the Tumorigenicity of Glioblastoma Tumor-Initiating Cells. *Cancer Discov*. 2016;6(5):532–545.

9. Nickoloff JA, Sharma N, Taylor L. Clustered DNA Double-Strand Breaks: Biological Effects and Relevance to Cancer Radiotherapy. *Genes* . 2020;11(1). https://doi.org/10.3390/genes11010099.

10. Trenner A, Sartori AA. Harnessing DNA Double-Strand Break Repair for Cancer Treatment. *Front Oncol*. 2019;9:1388.

11. Iliakis G, Mladenov E, Mladenova V. Necessities in the Processing of DNA Double Strand

Breaks and Their Effects on Genomic Instability and Cancer. *Cancers* . 2019;11(11). https://doi.org/10.3390/cancers11111671.

12. McClintock B. The behavior in successive nuclear divisions of a chromosome broken at meiosis. *Proc Natl Acad Sci U S A*. 1939;25(8):405–416.

13. Lo AWI, et al. DNA amplification by breakage/fusion/bridge cycles initiated by spontaneous telomere loss in a human cancer cell line. *Neoplasia*. 2002;4(6):531–538.

14. Li C, et al. Deciphering complex breakage-fusion-bridge genome rearrangements with Ambigram. *Nat Commun*. 2023;14(1):5528.

15. Schipler A, et al. Chromosome thripsis by DNA double strand break clusters causes enhanced cell lethality, chromosomal translocations and 53BP1-recruitment. *Nucleic Acids Res*. 2016;44(16):7673–7690.

16. Aguirre AJ, et al. Genomic Copy Number Dictates a Gene-Independent Cell Response to CRISPR/Cas9 Targeting. *Cancer Discov*. 2016;6(8):914–929.

17. Munoz DM, et al. CRISPR Screens Provide a Comprehensive Assessment of Cancer Vulnerabilities but Generate False-Positive Hits for Highly Amplified Genomic Regions. *Cancer Discov*. 2016;6(8):900–913.

18. Kosicki M, Tomberg K, Bradley A. Repair of double-strand breaks induced by CRISPR-Cas9 leads to large deletions and complex rearrangements. *Nat Biotechnol*. 2018;36(8):765–771.

19. Umbreit NT, et al. Mechanisms generating cancer genome complexity from a single cell division error. *Science*. 2020;368(6488). https://doi.org/10.1126/science.aba0712.

20. Kwon T, et al. Precision targeting tumor cells using cancer-specific InDel mutations with CRISPR-Cas9. *Proc Natl Acad Sci U S A*. 2022;119(9). https://doi.org/10.1073/pnas.2103532119.

21. Yang L, et al. Genome-wide inactivation of porcine endogenous retroviruses (PERVs). *Science*. 2015;350(6264):1101–1104.

22. Kuscu C, et al. CRISPR-STOP: gene silencing through base-editing-induced nonsense

mutations. *Nat Methods*. 2017;14(7):710–712.

23. Smith CJ, et al. Enabling large-scale genome editing at repetitive elements by reducing DNA nicking. *Nucleic Acids Res*. 2020;48(9):5183–5195.

24. Niu D, et al. Inactivation of porcine endogenous retrovirus in pigs using CRISPR-Cas9. *Science*. 2017;357(6357):1303–1307.

25. Yang H, et al. KLIPP - a precision CRISPR approach to target structural variant junctions in cancer. *bioRxiv*. 2023;2023.05.10.540176.

26. Teh SSK, et al. CRISPR-Cas9 for selective targeting of somatic mutations in pancreatic cancers. *NAR Cancer*. 2024;6(2):zcae028.

27. Ihry RJ, et al. p53 inhibits CRISPR-Cas9 engineering in human pluripotent stem cells. *Nat Med*. 2018;24(7):939–946.

28. Haapaniemi E, et al. CRISPR–Cas9 genome editing induces a p53-mediated DNA damage response. *Nat Med*. 2018;24(7):927–930.

29. Enache OM, et al. Cas9 activates the p53 pathway and selects for p53-inactivating mutations. *Nat Genet*. 2020;52(7):662–668.

30. Cancer of the Pancreas - Cancer Stat Facts [Internet]. *SEER*. https://seer.cancer.gov/statfacts/html/pancreas.html. Accessed February 7, 2023.

31. Kleeff J, et al. Pancreatic cancer. *Nat Rev Dis Primers*. 2016;2:16022.

32. AACR Project GENIE Consortium. AACR Project GENIE: Powering Precision Medicine through an International Consortium. *Cancer Discov*. 2017;7(8):818–831.

33. Baskar R, et al. Biological response of cancer cells to radiation treatment. *Front Mol Biosci*. 2014;1:24.

34. Bae S, Park J, Kim J-S. Cas-OFFinder: a fast and versatile algorithm that searches for potential off-target sites of Cas9 RNA-guided endonucleases. *Bioinformatics*. 2014;30(10):1473–1475.

35. Sedelnikova OA, Bonner WM. GammaH2AX in cancer cells: a potential biomarker for cancer diagnostics, prediction and recurrence. *Cell Cycle*. 2006;5(24):2909–2913.

36. Yu T, et al. Endogenous expression of phosphorylated histone H2AX in tumors in relation to DNA double-strand breaks and genomic instability. *DNA Repair (Amst)*. 2006;5(8):935–946.

37. Concordet J-P, Haeussler M. CRISPOR: intuitive guide selection for CRISPR/Cas9 genome editing experiments and screens. *Nucleic Acids Res*. 2018;46(W1):W242–W245.

38. IDT CRISPR-Cas9 gRNA checker [Internet]. https://www.idtdna.com/site/order/designtool/index/CRISPR_CUSTOM. Accessed September 28, 2023.

39. Graf R, et al. sgRNA Sequence Motifs Blocking Efficient CRISPR/Cas9-Mediated Gene Editing. *Cell Rep*. 2019;26(5):1098–1103.e3.

40. Brinkman EK, et al. Kinetics and Fidelity of the Repair of Cas9-Induced Double-Strand DNA Breaks. *Mol Cell*. 2018;70(5):801–813.e6.

41. Zou RS, et al. Massively parallel genomic perturbations with multi-target CRISPR interrogates Cas9 activity and DNA repair at endogenous sites. *Nat Cell Biol*. 2022;24(9):1433–1444.

42. Chen X, et al. Manta: rapid detection of structural variants and indels for germline and cancer sequencing applications. *Bioinformatics*. 2016;32(8):1220–1222.

43. Pannunzio NR, Watanabe G, Lieber MR. Nonhomologous DNA end-joining for repair of DNA double-strand breaks. *J Biol Chem*. 2018;293(27):10512–10523.

44. Patterson-Fortin J, D'Andrea AD. Exploiting the Microhomology-Mediated End-Joining Pathway in Cancer Therapy. *Cancer Res*. 2020;80(21):4593–4600.

45. Suzuki K, et al. Radiation-induced DNA damage and delayed induced genomic instability. *Oncogene*. 2003;22(45):6988–6993.

46. Puck TT, Marcus PI. Action of x-rays on mammalian cells. *J Exp Med*. 1956;103(5):653–666.

47. Cosper PF, et al. Chromosome Missegregation as a Modulator of Radiation Sensitivity. *Semin Radiat Oncol*. 2022;32(1):54–63.

48. Burgio G, Teboul L. Anticipating and Identifying Collateral Damage in Genome Editing. *Trends Genet*. 2020;36(12):905–914.

49. Berkovich E, Monnat RJ Jr, Kastan MB. Roles of ATM and NBS1 in chromatin structure modulation and DNA double-strand break repair. *Nat Cell Biol*. 2007;9(6):683–690.

50. Goldstein M, et al. Nucleolin mediates nucleosome disruption critical for DNA double-strand break repair. *Proc Natl Acad Sci U S A*. 2013;110(42):16874–16879.

51. Falco M, Masojć B, Sulikowski T. Radiotherapy in pancreatic cancer: To whom, when, and how? *Cancers (Basel)*. 2023;15(13). https://doi.org/10.3390/cancers15133382.

52. Payton M, et al. Small-molecule inhibition of kinesin KIF18A reveals a mitotic vulnerability enriched in chromosomally unstable cancers. *Nat Cancer*. 2024;5(1):66–84.

53. Chen Q, et al. Exploration of inhibitors targeting KIF18A with ploidy-specific lethality. *Drug Discov Today*. 2024;29(10):104142.

54. Al-Rawi DH, et al. Targeting chromosomal instability in patients with cancer. *Nat Rev Clin Oncol*. 2024;21(9):645–659.

55. Marquis C, et al. Chromosomally unstable tumor cells specifically require KIF18A for proliferation. *Nat Commun*. 2021;12(1):1–14.

56. Dewhurst SM. Chromothripsis and telomere crisis: engines of genome instability. *Curr Opin Genet Dev*. 2020;60:41–47.

57. Davoli T, de Lange T. Telomere-driven tetraploidization occurs in human cells undergoing crisis and promotes transformation of mouse cells. *Cancer Cell*. 2012;21(6):765–776.

58. Bae S, et al. Microhomology-based choice of Cas9 nuclease target sites. *Nat Methods*. 2014;11(7):705–706.

59. Yuan B, et al. Modulation of the microhomology-mediated end joining pathway suppresses

large deletions and enhances homology-directed repair following CRISPR-Cas9-induced DNA breaks. *BMC Biol*. 2024;22(1):101.

60. Owens DDG, et al. Microhomologies are prevalent at Cas9-induced larger deletions. *Nucleic Acids Res*. 2019;47(14):7402–7417.

61. Liu J, Erenpreisa J, Sikora E. Polyploid giant cancer cells: An emerging new field of cancer biology. *Semin Cancer Biol*. 2022;81:1–4.

62. Moein S, et al. Cancer regeneration: Polyploid cells are the key drivers of tumor progression. *Biochim Biophys Acta Rev Cancer*. 2020;1874(2):188408.

63. Coward J, Harding A. Size Does Matter: Why Polyploid Tumor Cells are Critical Drug Targets in the War on Cancer. *Front Oncol*. 2014;4:123.

64. Cortés-Ciriano I, et al. Comprehensive analysis of chromothripsis in 2,658 human cancers using whole-genome sequencing. *Nat Genet*. 2020;52(3):331–341.

65. Mardin BR, et al. A cell-based model system links chromothripsis with hyperploidy. *Mol Syst Biol*. 2015;11(9):828.

66. Mahmoud M, et al. Structural variant calling: the long and the short of it. *Genome Biol*. 2019;20(1):246.

67. Bowland K, et al. Islands of genomic stability in the face of genetically unstable metastatic cancer. *PLoS One*. 2024;19(12):e0298490.

68. Bulcha JT, et al. Viral vector platforms within the gene therapy landscape. *Signal Transduct Target Ther*. 2021;6(1):53.

69. Butt MH, et al. Appraisal for the potential of viral and nonviral vectors in gene therapy: A review. *Genes (Basel)*. 2022;13(8):1370.

70. Kachanov A, et al. The menace of severe adverse events and deaths associated with viral gene therapy and its potential solution. *Med Res Rev*. 2024;44(5):2112–2193.

71. Fontana M, et al. CRISPR-Cas9 gene editing with nexiguran ziclumeran for ATTR

cardiomyopathy. *N Engl J Med*. 2024;391(23):2231–2241.

72. Cohn DM, et al. CRISPR-based therapy for hereditary angioedema. *N Engl J Med*. 2025;392(5):458–467.

73. Longhurst Hilary J., et al. CRISPR-Cas9 In Vivo Gene Editing of KLKB1 for Hereditary Angioedema. *N Engl J Med*. 2024;390(5):432–441.

74. Dreaden EC, et al. RNA-Peptide nanoplexes drug DNA damage pathways in high-grade serous ovarian tumors. *Bioeng Transl Med*. 2018;3(1):26–36.

75. Isaac I, et al. Reengineering endogenous targeting lipid nanoparticles (ENDO) for systemic delivery of mRNA to pancreas. *Adv Mater*. 2025;e2507657.

76. Mandalawatta HP, et al. Emerging trends in virus and virus-like particle gene therapy delivery to the brain. *Mol Ther Nucleic Acids*. 2024;35(3):102280.

77. Oieni J, et al. Nano-ghosts: Novel biomimetic nano-vesicles for the delivery of antisense oligonucleotides. *J Control Release*. 2021;333:28–40.

78. Tsilimigras DI, et al. Liver metastases. *Nat Rev Dis Primers*. 2021;7(1):27.

79. Robinson JT, et al. Integrative genomics viewer. *Nat Biotechnol*. 2011;29(1):24–26.

80. Pinello L, et al. Analyzing CRISPR genome-editing experiments with CRISPResso. *Nat Biotechnol*. 2016;34(7):695–697.

81. Van der Auwera GA, O'Connor BD. *Genomics in the Cloud*. O'Reilly Media, Inc.; .

82. Cingolani P, et al. A program for annotating and predicting the effects of single nucleotide polymorphisms, SnpEff: SNPs in the genome of Drosophila melanogaster strain w1118; iso-2; iso-3. *Fly* . 2012;6(2):80–92.

83. Joung J, et al. Genome-scale CRISPR-Cas9 knockout and transcriptional activation screening. *Nat Protoc*. 2017;12(4):828–863.

84. Li W, et al. MAGeCK enables robust identification of essential genes from genome-scale CRISPR/Cas9 knockout screens. *Genome Biol*. 2014;15(12):554.

FIGURES

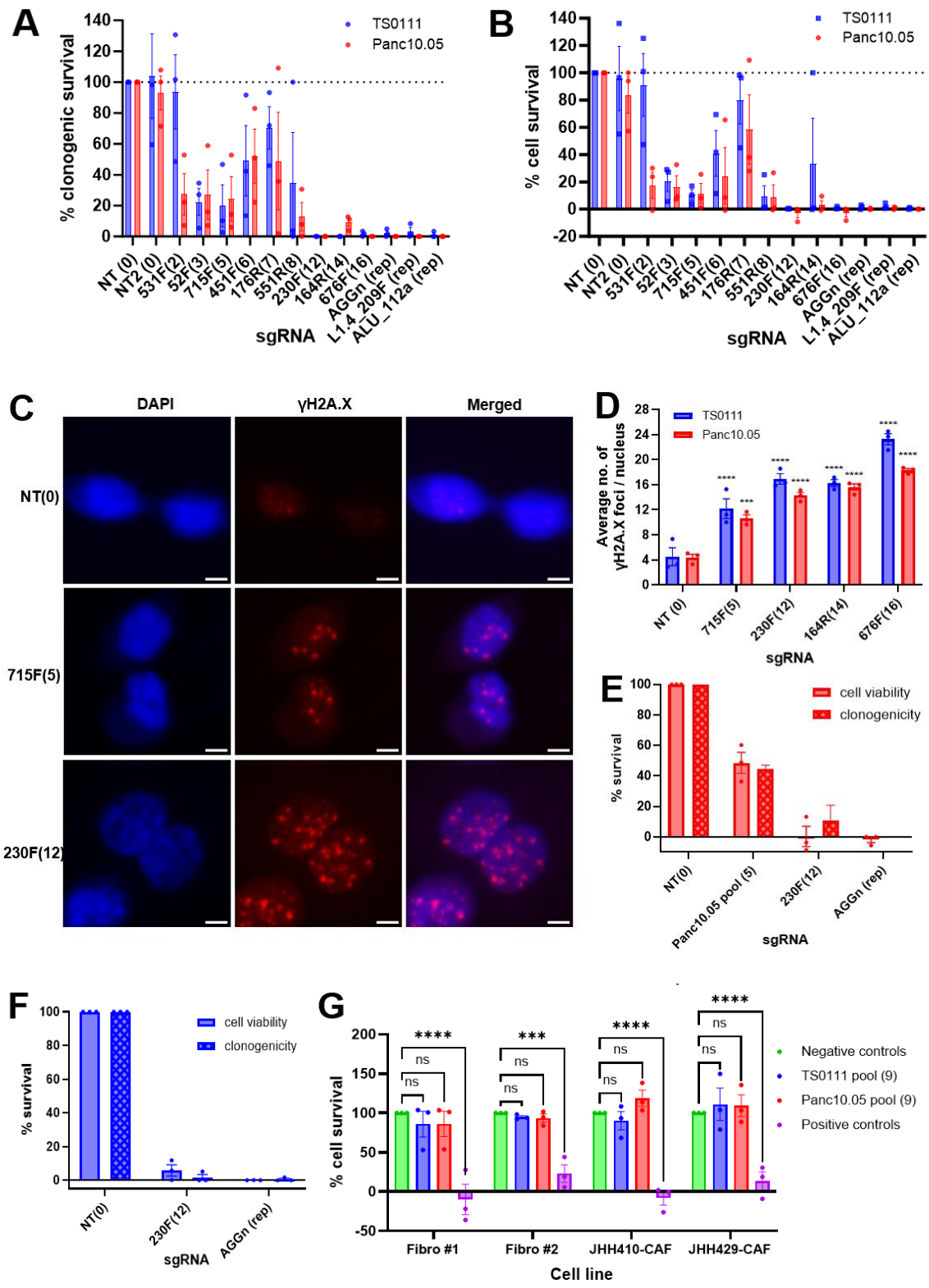

Figure 1. Increased CRISPR-Cas9-induced double strand breaks (DSBs) inhibited cancer cell growth. **(A)** Clonogenic survival with increased number of CRISPR-Cas9 target sites in the human genome of two pancreatic cancer (PC) cell lines. Number of target sites in parentheses, "rep" indicates repetitive element-targeting. N=3; mean ± SEM, normalized to NT. **(B)** Cell survival with increased number of CRISPR-Cas9 target sites as detected by alamarBlue cell viability assay. N=3; mean ± SEM, normalized to NT. **(C)**

Representative images of γH2A.X staining in Panc10.05 cells transduced with either non-targeting (NT), 715F(5), or 230F(12) multi-target sgRNAs. Images were acquired at 40X magnification. Scale bar is 5μM. **(D)** Number of γH2A.X foci as a function of the number of CRISPR-Cas9 target sites. >100 nuclei were analyzed for each condition. Dunnett's test between NT and each multi-target sgRNA; *** *P<0.001,* **** *P<0.0001.* N=3; mean ± SEM. **(E)** Clonogenic and cell survival 21 days after electroporating in CRISPR-Cas9 with multi-target sgRNAs or a pool of 5 sgRNAs targeting different noncoding mutations in the Panc10.05 genome. N=2/3; mean ± SEM, normalized to NT. **(F)** Clonogenic and cell survival of TS0111 cells 21 days after electroporating in CRISPR-Cas9 containing multi-target sgRNAs. N=3; mean ± SEM, normalized to NT. **(G)** Cell survival of two primary skin fibroblasts lines (Fibro #1 and Fibro #2) and two cancer-associated fibroblasts lines (JHH410-CAF and JHH429-CAF) one month after the transduction of lentivirus pools containing 9 sgRNAs targeting different non-coding mutations specific to TS0111 (TS0111 pool) and Panc10.05 (Panc10.05 pool). Dunnett's test between negative controls and each treatment group; *** *P<0.001,* **** *P<0.0001.* N=3; mean ± SEM, normalized to NT.

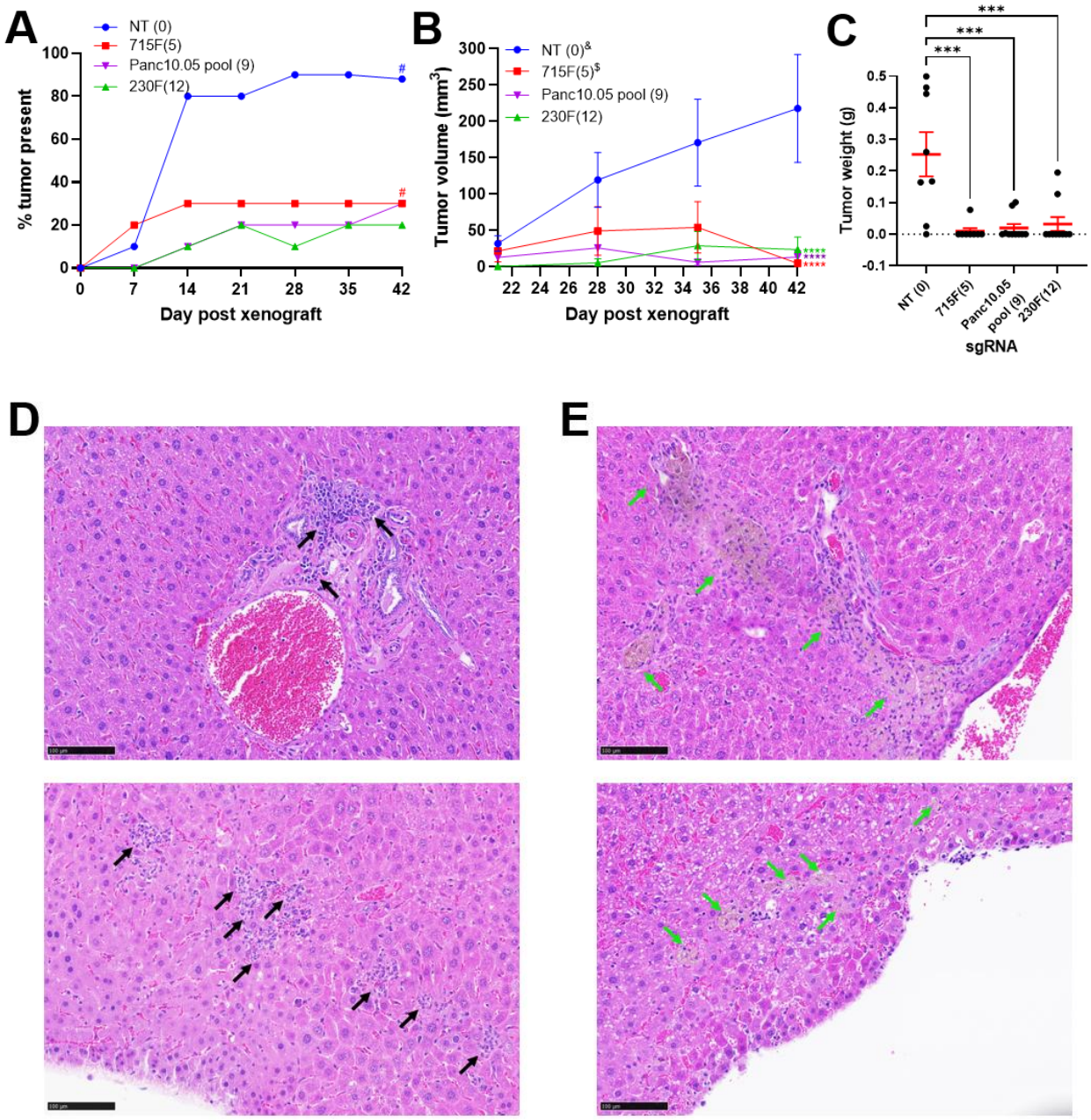

Figure 2. Simultaneous CRISPR-Cas9 targeting inhibited tumor growth.
(A-C) Tumor growth experiment in subcutaneous xenograft models. Panc10.05 Cas9-expressing cells transduced with the following sgRNAs: NT, 715F(5), 230F(12), or a pool of 9 sgRNAs targeting different noncoding mutations unique to Panc10.05 (Panc10.05 pool) were injected into athymic, nude mice for tumor growth. **(A)** Percentage of tumors present post xenograft. # indicates absence of two data points due to early death around week 5 (33-36 days). **(B)** Tumor volume measurements post xenograft. Dunn-Sidak test between NT and the other treatment groups on week 6, all $P<0.0001$. N=10; mean ± SEM. & indicates absence of week 5 and 6 data points of two tumors due to early death. $ indicates absence of two data points from week 6 due to early death. **(C)** Tumor weight measurements on week 6 post xenograft. Dunnett's test between NT (N=8) and 715F(5): $P=0.0003$ (N=8), 230F(12): $P=0.0008$ (N=10), and Panc10.05 pool: $P=0.0004$ (N=10). Mean ± SEM was shown. **(D-E)** Metastatic growth experiment in hemi-spleen injection mouse models of liver metastasis. Hematoxylin and eosin (H&E) staining of the liver sections of mice treated with **(D)** NT or **(E)** 230F(12) sgRNA-expressing PC cells. Black arrow: tumor growth; green arrow: tumor regression. The top and bottom panels represent liver sections from two different mice of the same treatment group. Images were acquired at 20X magnification. Scale bar is 100μM.

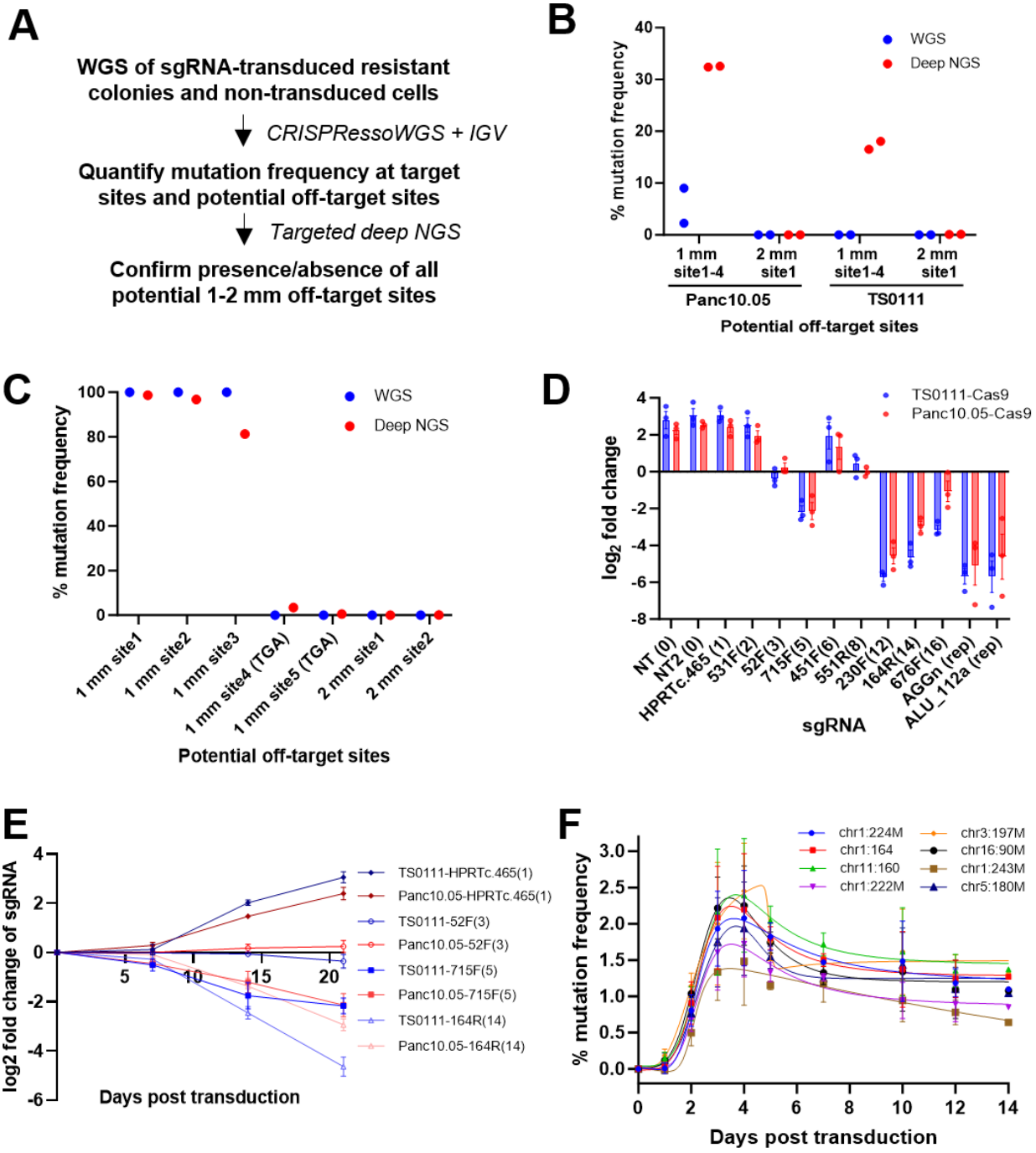

Figure 3. Multiple CRISPR-Cas9 scissions led to delayed cell death.
(A) Analysis workflow for quantification of on- and off-target sites in resistant colonies from clonogenicity assays. **(B-C)** Comparisons of mutation frequency at 1-2 mismatch (mm) sites detected by whole genome sequencing (WGS) and targeted deep next generation sequencing (deep NGS) in resistant colonies. **(B)** 531F(2) sgRNA-resistant colonies. All four 1mm sites were sequenced using the same primers. N=2, mean ± SEM. **(C)** Panc10.05 164R(14) sgRNA-resistant colony. Non-canonical PAMs were indicated in parentheses. N=1. **(D)** Fold change of multi-target sgRNAs in two PC cell lines 21 days after transduction. Number of target sites in parentheses, "rep" indicates repetitive element-targeting. N=3; mean ± SEM. **(E)** sgRNA tag survival as a function of time. N=3; mean ± SEM. **(F)** Mutation frequencies of eight 164R(14) sgRNA target sites in Panc10.05 Cas9-expressing cells at various time points. N=3; mean ± SEM. Bell-shaped least squares regression; R^2 = 0.42-0.80. Relatively low percentages were due to the absence of antibiotic selection of transduced cells.

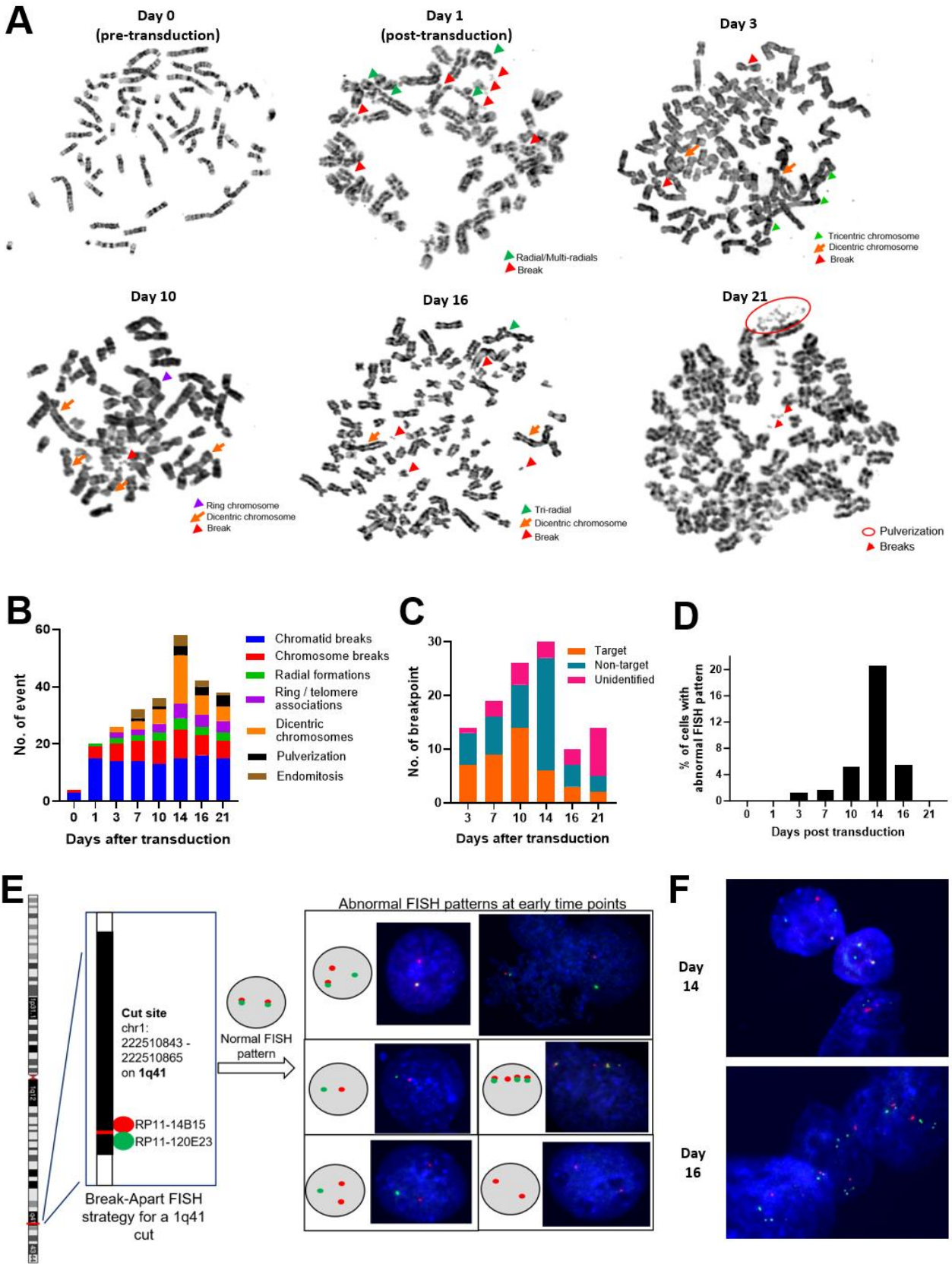

Figure 4. Ongoing and extreme chromosomal instability (CIN) in multi-target sgRNA transduced cells.

TS0111 Cas9-expressing cells were transduced with 164R(14) sgRNA and subjected to **(A-C)** chromosome breakage assays and **(D-F)** break-apart FISH assays. **(A)** Metaphase images of representative cells pre- and

post-transduction of sgRNA. Karyotypic alterations are labeled. **(B)** Cytogenetic changes (events per 100 metaphase cells) as a function of time. **(C)** Quantification of breakpoints on dicentric, tricentric, and ring chromosomes, categorized by their chromosomal band locations to determine whether the breakpoint junction was located at 164R(14) sgRNA targeted or non-targeted regions. **(D)** Percentage of cells with rearrangements at 1q41 detected by break-apart FISH assay as a function of time. **(E)** Break-apart FISH strategy at the 1q41 cut site. Abnormal FISH patterns were shown using cells collected at early time points. DNA was stained with DAPI. **(F)** Complex rearrangements were observed in cells on 14 and 16 days after transduction.

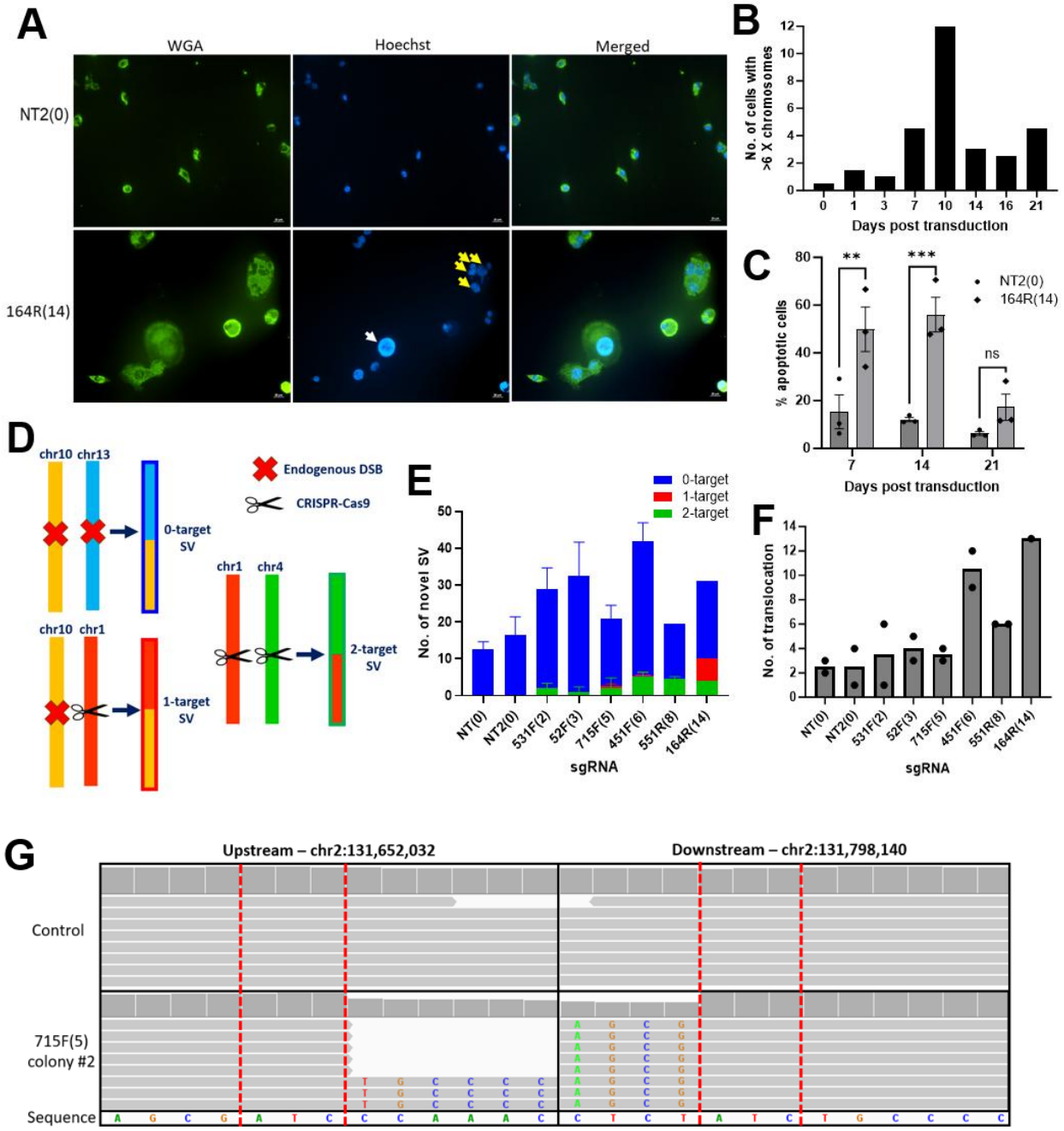

Figure 5. Peak polyploidy and chromosomal rearrangements in multi-target sgRNA transduced cells. **(A)** Shown are Panc10.05 cells transduced with NT2 (non-targeting) or 164R(14) and stained with wheat germ agglutinin (WGA; green) and Hoechst 33342 (blue) 14 days after transduction. White arrow: large nucleus; yellow arrows: multiple nuclei in a cell. **(B)** Number of TS0111 transduced cells with >6 X chromosomes over time using XY FISH. **(C)** Apoptosis analysis of Panc10.05 cells after treatment with 164R(14) or NT2 using Annexin V flow cytometry assay. Sidak's multiple comparisons test, day 7: *P=0.005,* day 14: *P=0.0008,* and day 21: *P=0.53*. N=3; mean ± SEM. **(D)** Structural variants (SVs) were categorized by whether the breakpoints resulted from 2 sites that were CRISPR-Cas9 targeted (2-target SV), 1 site that was targeted (1-target SV), or both sites arising from endogenous DSBs (0-target SV). **(E)** Quantification of SVs through WGS analyses of Panc10.05 surviving/resistant colonies after treatment with multi-target sgRNAs. N=2 except for 164R(14) (N=1); mean ± SEM. **(F)** Number of translocation detected in each Panc10.05 surviving colony. N=2 except for 164R(14) (N=1); mean ± SEM. **(G)** Example of a novel 0-target deletion from a 715F(5) sgRNA-resistant colony. The red dotted lines indicate the 3bp homology region on both upstream and downstream sequences.

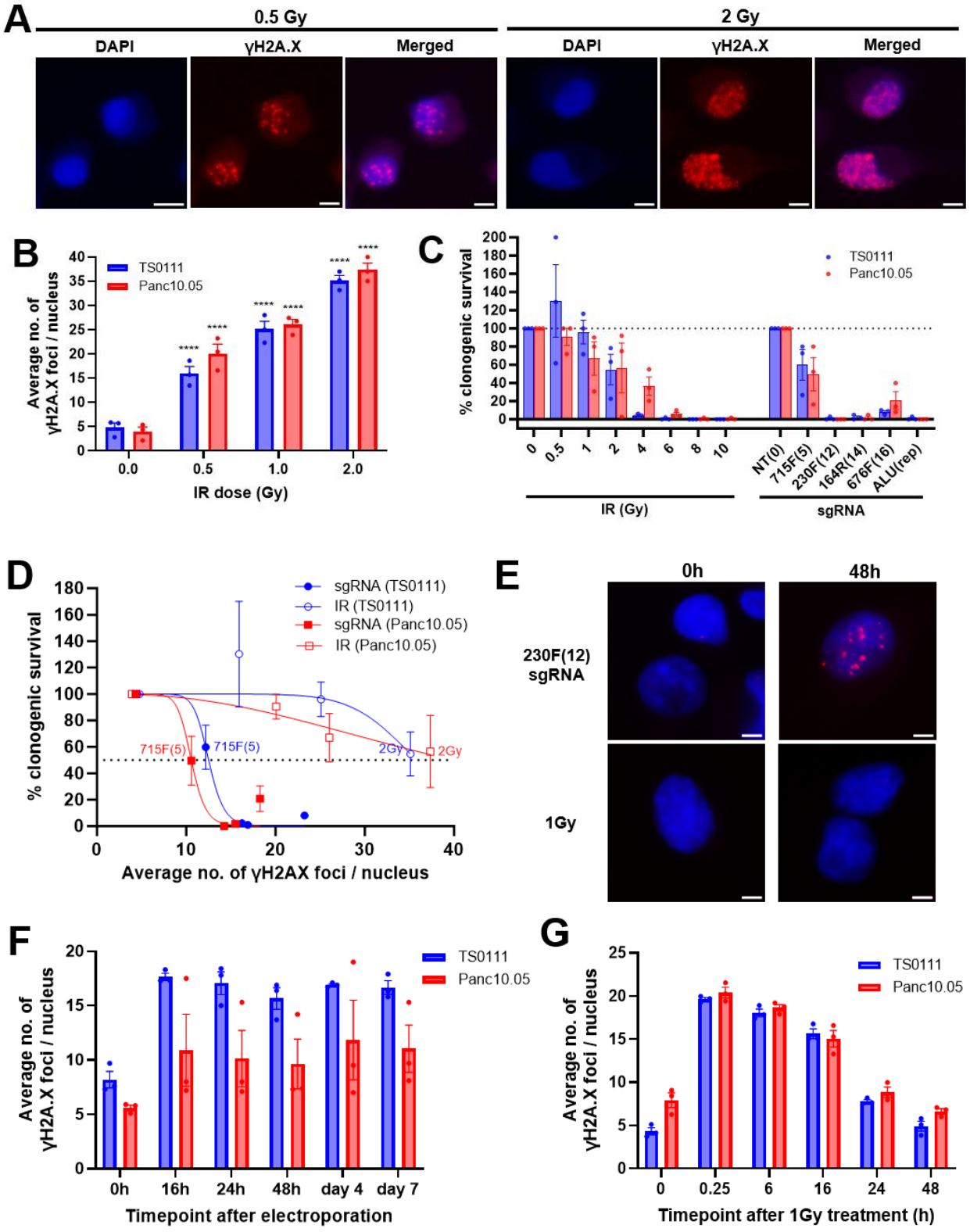

Figure 6. CRISPR-Cas9-induced DSBs were more cytotoxic than irradiation (IR)-induced DSBs. **(A)** Representative images of γH2A.X staining in TS0111 cells irradiated with 0.5 Gy and 2 Gy. Images were acquired at 40X magnification. Scale bar is 5μM. **(B)** Number of γH2A.X foci as a function of IR dose. >100 nuclei were analyzed for each condition. Dunnett's test between 0 Gy and each dose; **** *P<0.0001.* N=3; mean ± SEM. **(C)** Clonogenic survival as a function of IR dose or number of target sites of sgRNAs over 21 days. N=3; mean ± SEM, normalized to 0 Gy or NT. **(D)** Clonogenic survival with increased number of γH2A.X foci detected in IR- and sgRNA-treated cells. N=3; mean ± SEM, nonlinear regressions were

shown **(E)** Representative merged images of γH2A.X staining in TS0111 cells treated with CRISPR-Cas9 RNP containing 230F(12) sgRNA or 1Gy at 0- and 48-hour timepoint. Images were acquired at 40X magnification. Scale bar is 5μM. **(F-G)** Number of γH2A.X foci as a function of time after **(F)** electroporating in CRISPR-Cas9 RNP containing 230F(12) sgRNA or **(G)** irradiated with 1Gy. >100 nuclei were analyzed for each condition. N=3; mean ± SEM.

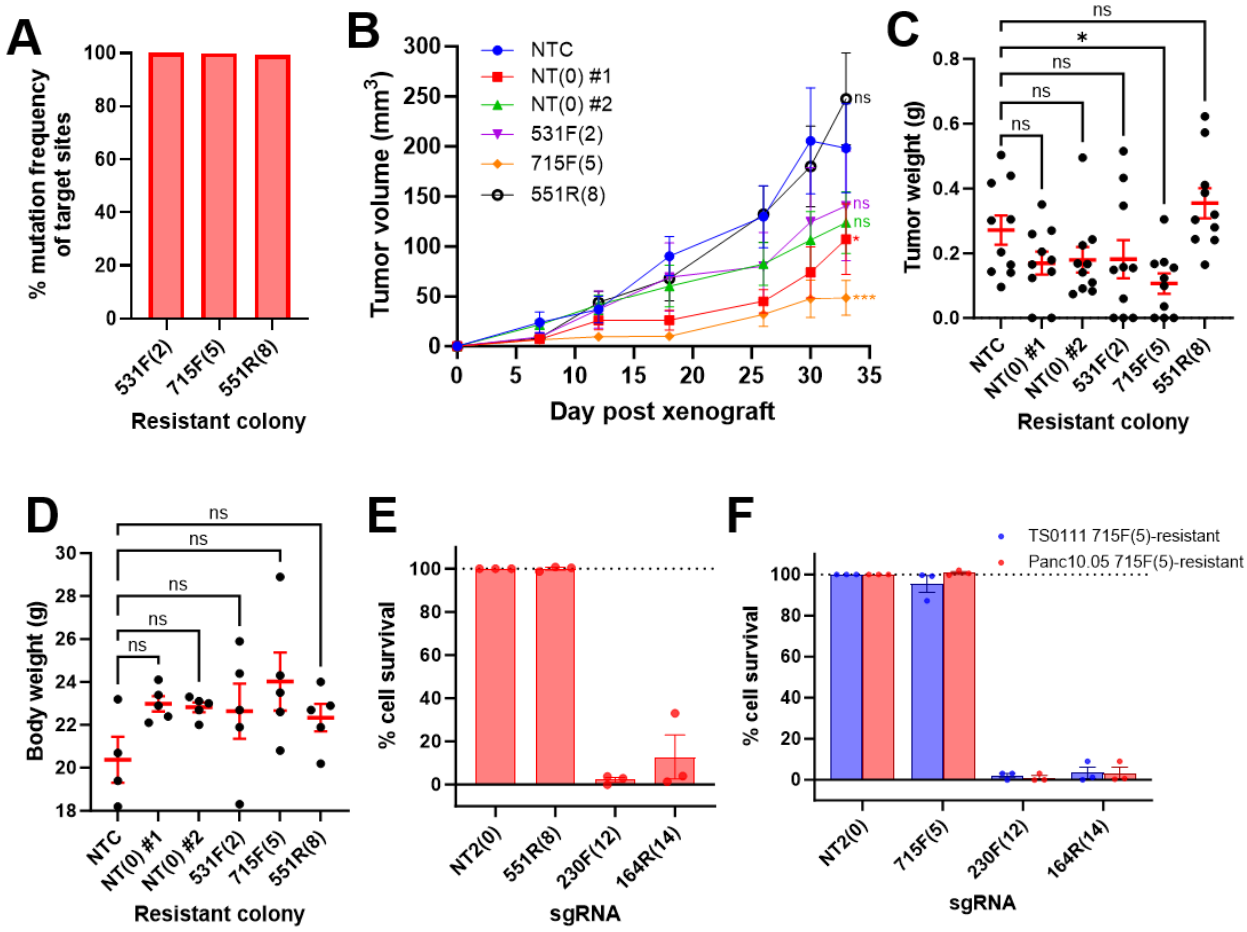

Figure 7. Cells resistant to one sgRNA were susceptible to other sgRNAs.
(A) Mutation frequency of sgRNA target sites in each CRISPR-Cas9 surviving colony used for xenograft experiment. **(B-D)** Tumor growth experiment of CRISPR-Cas9 surviving colonies in subcutaneous xenograft models. In addition to a non-transduced cell line (NTC), surviving colonies from clonogenicity experiment (Figure 1A) transduced with non-targeting sgRNA (NT colony #1 and NT colony #2) and multitarget sgRNAs (531F(2), 715F(5), 551R(8)) were injected into athymic, nude mice for tumor growth. **(B)** Tumor volume measurements post xenograft. Dunnett's test between NTC and NT #1: *P=0.050*, NT #2: *P=0.145*, 531F(2): *P=0.349*, 715F(5): *P=0.0002*, 551R(8): *P=0.498* on week 5. N=10 (N=8 for NTC on day 30 and 33 due to early death); mean ± SEM. **(C)** Tumor weight measurements. Dunnett's test between NTC and NT #1: *P=0.341*, NT #2: *P=0.437*, 531F(2): *P=0.457,* 715F(5): *P=0.041*, and 551R(8): *P=0.531*. N=10; mean ± SEM. **(D)** Body weight of mice 5 weeks post xenograft. Dunn-Sidak test between NTC and the other treatment groups showed no significant differences. N=5 except for NTC (N=4 due to early death); mean ± SEM. **(E)** Cell survival of Panc10.05 551R(8)-resistant colony that was re-transduced with non-targeting sgRNA (NT2) or multi-targeting sgRNAs (551R(8), 230F(12), and 164R(14)), as detected by alamarBlue cell viability assay and normalized to NT2. N=3; mean ± SEM. **(F)** Cell survival of TS0111 and Panc10.05 715F(5)-resistant colony that was re-transduced with non-targeting sgRNA (NT2) or multi-targeting sgRNAs (715F(5), 230F(12), and 164R(14)), as detected by alamarBlue cell viability assay and normalized to NT2. N=3; mean ± SEM.

TABLE

Table 1. Number of CRISPR-Cas9-induced DSBs from WGS of surviving TS0111 and Panc10.05 colonies.

sgRNA	Number of predicted perfect target sites[1]	Number of potential off-target sites (1 mm - 2 mm)[2]	Number of mutated sites in TS0111 (0 mm - 1 mm - 2 mm)[3]	Number of mutated sites in Panc10.05 (0 mm - 1 mm - 2 mm)[3]
NT	0	0-1	0-0-0	0-0-0
NT2	0	0-0	0-0-0	0-0-0
531F(2)	2	4-1	2-0-0	2-0-0
52F(3)	3	0-0	3-0-0	3-0-0
715F(5)	5	2-1	5-1-0[4]	5-1-0
451F(6)	6	0-1	6-0-0	6-0-0
176R(7)	7	2-1	6-1-0	6-0-0
551R(8)	8	2-1	NA	7-0-0
230F(12)	12	8-1	NA	NA
164R(14)	14	5-2	NA	13-3-0[4]
676F(16)	16	2-6	16-1-0	NA

1. Number of perfect matches in CRISPOR using the GRCh38 human reference genome, including both canonical (NGG) and non-canonical (NGA/NAG) PAMs. 2. From CRISPOR, number of 1 and 2 mismatches (1 mm - 2 mm). 3. Matched or mismatched sites that were mutated from WGS analyses of two resistant colonies for each sgRNA, using an average variant allele frequency cutoff of 10%. Numbers are shown as 0 mm - 1 mm - 2 mm. 4. Only one colony could be obtained. NA: Resistant colonies could not be obtained.

SUPPLEMENTAL MATERIAL

Supplemental Methods

Supplemental Figure 1-9

Supplemental Table 1-5

Supplemental Data 1

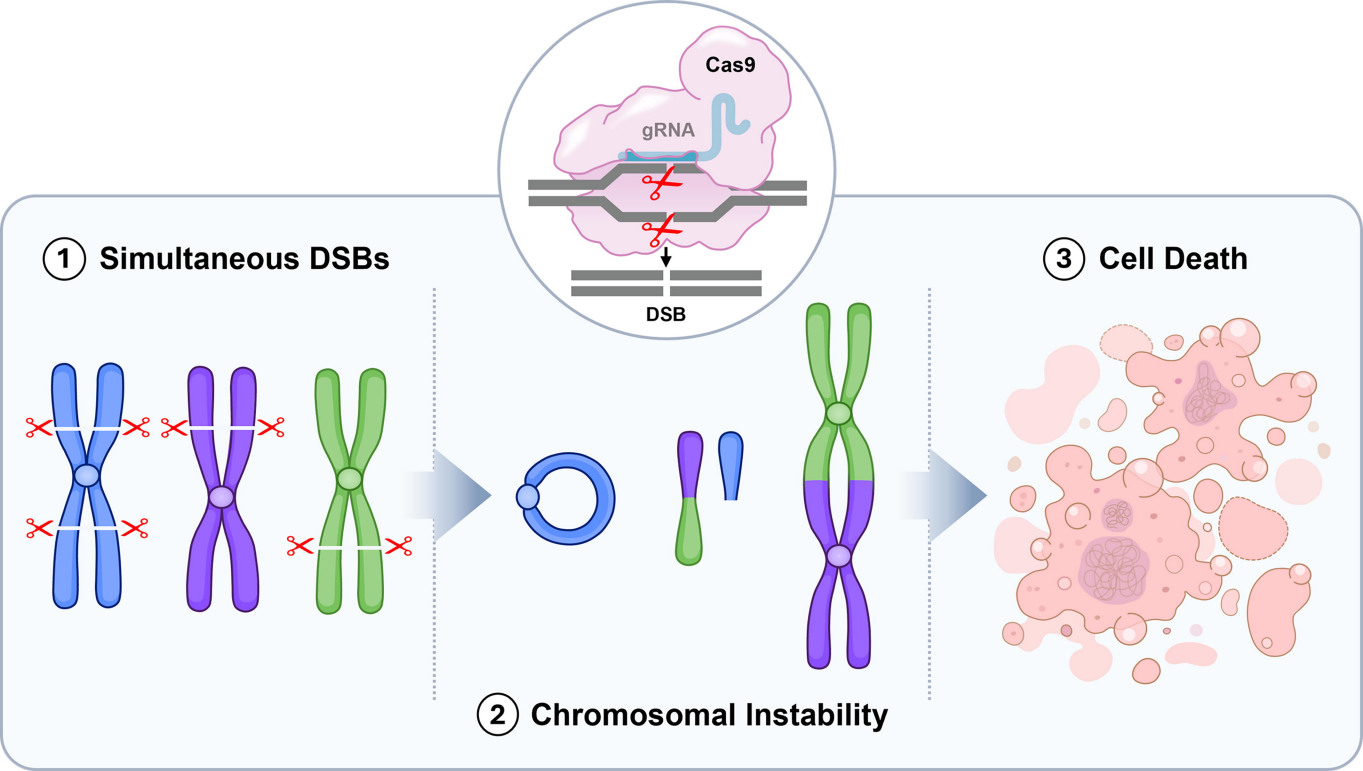
Cas9
gRNA
DSB
1 Simultaneous DSBs
2 Chromosomal Instability
3 Cell Death